## Title

Investigation of Small Molecule Dynamics Using Fast Beam Photofragment Spectroscopy and Flat Liquid Jet Scattering



## Author

Saric, Steven R

## Publication Date

2023

Peer reviewed|Thesis/dissertation

# Investigation of Small Molecule Dynamics Using Fast Beam Photofragment Spectroscopy and Flat Liquid Jet Scattering

By

Steve Saric

A dissertation submitted in partial satisfaction of the

requirements for the degree of

Doctor of Philosophy

in

Chemistry

in the

Graduate Division

of the

University of California, Berkeley

Committee in charge:

Professor Daniel M. Neumark, Chair
Professor Richard Saykally
Professor Hartmut Haeffner

Fall 2023

Investigation of Small Molecule Dynamics Using Fast Beam Photofragment Spectroscopy and Flat Liquid Jet Scattering

# Abstract

## Investigation of Small Molecule Dynamics Using Fast Beam Photofragment Spectroscopy and Flat Liquid Jet Scattering

By

Steve Saric

Doctor of Philosophy in Chemistry

University of California, Berkeley

Professor Daniel M. Neumark, Chair

Molecular dynamics is the sub-field of chemistry interested in studying the microscopic movements of molecules and their partitioning of energy. Through molecular dynamics, a higher level of understanding of both reactive and non-reactive chemical processes can be achieved. In these works, two separate techniques are used to investigate the molecular dynamics of three different chemical systems. The first technique, fast beam photodissociation spectroscopy utilizes a combination of anion photoelectron spectroscopy and fast beam free radical dissociation to study the photodissociation dynamics of free radical species. The free radical species investigated in these works are the methyl phenoxy radical and isoprene hydroxy radical both of which are relevant to atmospheric and combustion chemistry. Insights are obtained for the different dissociation products which can be formed from these two radicals, the branching ratios of each dissociation channel, and the dissociation mechanisms responsible for each channel. The second technique, flat liquid jet scattering is used to investigate the gas-liquid interface of $ND_3$ and dodecane. Flat liquid jet scattering is a relatively new technique which utilizes a flat liquid sheet and molecular beam to uncover mechanistic details of gas-liquid interactions. The dynamics uncovered in these works specifically investigate $ND_3$ scattered from the relatively high vapor pressure liquid dodecane, and provide a proof of concept for the flat liquid jet technique being used on more volatile liquids such as water.

For my mother and sister. Your support and encouragement have inspired me to continue where I would have otherwise given up!

# Contents

# Chapter 1: Introduction

## 1.2 Molecular Dynamics

Molecular dynamics is a field interested in the study of the microscopic movements and energy partitioning of molecules.[1] Both experimental and theoretical techniques to probe the dynamics of molecules and chemical reactions have been developed since the early 1960's.[2-5] These techniques have led to unprecedented levels of detail in the fundamental understanding of both reactive and non-reactive molecular motion which has played a significant role in countless fields including atmospheric chemistry, environmental science, biochemistry, and chemical engineering.[1, 6-10]

The development of molecular beam experiments in particular has been important to the understanding of molecular dynamics in a wide variety of fields.[11, 12] For more than thirty years, our research group has made use of various molecular beam experiments to study the molecular dynamics of many systems relevant in physics, chemistry, and biology.[13-16]

The works described in this dissertation make use of two techniques, both of which are designed to study the dynamics of a particular class of molecules. The first technique that is described in this work is fast beam photofragment spectroscopy which is designed to study the dynamics of free radical species relevant to atmospheric and combustion chemistry. In this work, fast beam photofragment spectroscopy is used to study the dynamics of two free radical species, methyl phenoxy and isoprene hydroxy. The second technique utilized in these works is flat liquid jet scattering, a recently developed technique used to probe the dynamics of the gas-liquid interface. Flat liquid jet scattering is used to investigate the non-reactive dynamics of $ND_3$ on a dodecane liquid surface, which serves as a proof of concept and necessary steppingstone in the development of this technique.

## 1.1 Photodissociation Reactions

Photodissociation reactions are unimolecular reactions that involve the absorption of a photon by a molecule and the subsequent dissociation of that molecule into products. A general example of a photodissociation reaction is shown in equation 1.

$$\mathrm{ABC} \xrightarrow{h\nu} \mathrm{AB} + \mathrm{C} \qquad (1)$$

The mechanisms and dynamics of photodissociation reactions can be investigated through the characterization of the product fragments. While equation 1 shows a possible reaction for the photodissociation of species ABC, it does not display all the potential product channels for this molecule. Other possible reactions of species ABC are shown in equations 2-4.

$$\mathrm{ABC} \xrightarrow{h\nu} \mathrm{AC} + \mathrm{B} \qquad (2)$$

$$ABC \xrightarrow{h\nu} BC + A \quad (3)$$

$$ABC \xrightarrow{h\nu} A + B + C \quad (4)$$

Characterizing the masses of the products allows for identification of which channels are seen for the actual dissociation of a molecule, and the branching ratios for each channel.[15, 17, 18]

Characterizing the translational energy of the fragments can give insight into the potential energy surface of the molecule and the dynamics taking place during photodissociation. Two limiting mechanisms for photodissociation reactions differ by the identity of the excited state potential energy surface. During photodissociation, the molecule will absorb a photon and be moved from a ground state potential energy surface to an excited state potential energy surface that may be bound or repulsive.[19] Excitation into a repulsive potential energy surface leads to rapid dissociation along the reaction coordinate. Conversely, excitation into a bound potential energy surface results in either predissociation where a repulsive potential energy surface crosses over the bound excited state, or internal conversion to the ground state followed by statistical dissociation.[19] A representation of the these three mechanisms is shown in Fig. 1.2.1.

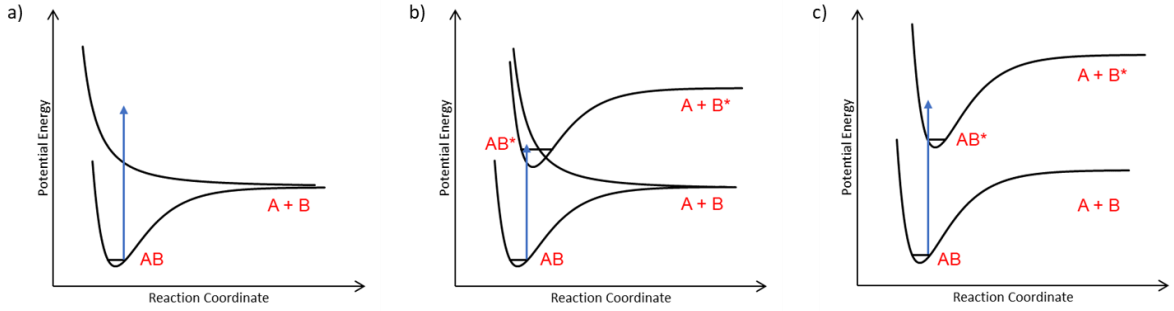


**Figure 1.2.1.** Potential energy surfaces for a) a repulsive excited state dissociation, b) an excited state predissociation, and c) a ground state dissociation process for the molecule AB dissociating to products A + B. The repulsive excited state results in rapid translation along the reaction coordinate and dissociation taking place on the excited state surface. Predissociation excites the molecule to a bound excited state, which crosses over a repulsive excited state where dissociation can occur along the reaction coordinate. The ground state process requires internal conversion to the ground state followed by statistical dissociation.

Repulsive potential energy surfaces lead to dissociation taking place on the excited state surface due to potential energy being converted to translational energy along the reaction coordinate. For this reason, excited state dissociation results in most of the available energy being partitioned into translational energy. In contrast, ground state dissociation results in most of the available energy being partitioned into the internal degrees of freedom of the products (vibrations and rotations).[19] By comparing the maximum available energy to an experimentally measured translational energy, it is possible to gain insight into the mechanism of dissociation

that is occurring. An example of each limiting mechanism from our prior work is provided in Fig. 1.2.2. Panel a) of Fig. 1.2.2 is the dissociation of iso-propoxy to OH and $C_3H_6$ at 248 nm which represents a ground state dissociation process, the blue arrow points to the maximum translational energy that is significantly larger than the distribution peak.[18] Panel b) of Fig. 1.2.2 is the dissociation of $CH_3OO$ to $CH_3O$ and O ($^1D$) at 248 nm, which represents an excited state dissociation process, the red line represents the maximum translational energy that is very near the peak of the distribution.[18, 20]

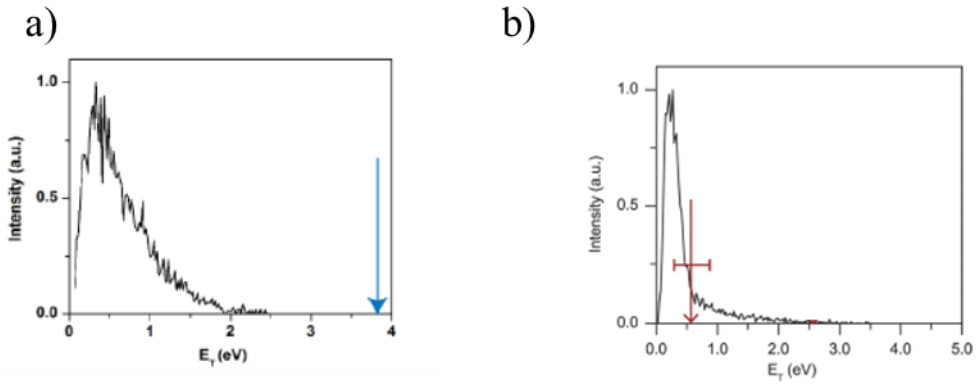


**Figure 1.2.2.** The translational energy distributions for a) iso-propoxy dissociation to OH and $C_3H_6$ at 248 nm, and b) $CH_3OO$ to $CH_3O$ and O ($^1D$) at 248 nm. The maximum translational energies are marked by a blue arrow and red arrow in distributions a and b respectively. Distribution a has a maximum translational energy that is far above the peak of the distribution which is representative of a ground state dissociation process. Distribution b has a maximum translational energy that is very close to the peak of the distribution and is representative of an excited state dissociation process.[18, 20]

Another measurable factor that can give insights into the mechanism of dissociation is the degree of anisotropy of the products. By measuring an angular distribution of the products, the anisotropy parameter $\beta$ can be determined using equation 2.

$$P(E_T, \theta) = P(E_T) \cdot [1 + \beta(E_T) P_2(cos\theta)] \quad (5)$$

Here $\beta(E_T)$ is the translational energy anisotropy parameter and $P_2(cos\theta)$ is the second Legendre polynomial.[21] Anisotropy parameters for this work are measured using a non-polarized excimer laser which leads to values of -1 to 1/2 for parallel and perpendicular transitions respectively.[22] An anisotropy parameter of 0 has no angular dependence and results in an isotropic distribution. Since the molecule has time to rotate before falling apart, isotropic distributions are indicative of ground state dissociation. A highly anisotropic distribution on the other hand requires a rapid dissociation process which is indicative of excited state dissociation.[22] It is important to note that the non-polarized laser used in our work is not a typical case, and in the case of a linearly polarized laser the $\theta$ parameter is defined differently. In the

linearly polarized case, $\theta$ is defined as the angle between the electric field vector and dissociation recoil axis, while in our experiment $\theta$ is defined as the angle between the laser propagation direction and the dissociation recoil axis. The linearly polarized case leads to anisotropy parameters ranging from -1 to 2 for perpendicular and parallel transitions respectively.

## 1.2 Free Radicals

The photodissociation reactions studied in this work are those of free radical species. Free radicals are highly reactive chemical species containing unpaired electrons. Due to their highly reactive nature, they often play a significant role in many chemical and biological processes. Unlike closed shell molecules, free radicals have lower-lying electronic states and low dissociation energies leading to interesting dissociation dynamics.[23, 24] Atmospheric and combustion chemistry in particular are two fields where free radical species play a significant role in many of the relevant reactions.[23] While free radicals are a particularly interesting class of molecules to investigate, their transient nature makes them difficult to study. However, the fast radical beam machine (FRBM) used during our photodissociation experiments makes use of anion photodetachment to create and study these species.

Understanding the photodissociation dynamics of combustion and atmospherically relevant free radicals has been a goal of our research group for many years and has led to the elucidation of fundamental mechanisms in many classes of molecules such as alkoxy radicals, peroxy radicals, and perthiyl radicals.[14, 20, 24-27] The works presented in this dissertation, investigate the photodissociation dynamics of two atmospherically relevant free radical species using fast beam photofragment spectroscopy. Methyl phenoxy is presented in chapter 3 and isoprene hydroxy is presented in chapter 4.

## 1.3 Gas-Liquid Interface

The gas-liquid interface is relevant to countless natural processes including aerosol formation, ocean acidification, and acid rain formation.[28-31] While significant work has been done previously to study the gas–liquid interface, elucidation of mechanistic detail behind gas–liquid interactions has remained a challenging endeavor.[32] Recent efforts by Nathanson and others, however, have allowed for the use of molecular beam scattering to study the gas–liquid interface[32-34]. This has uncovered mechanistic detail at a degree greater than what was previously possible for this critical chemical environment.

Molecular beam scattering is an incredibly powerful technique that has been used for over half a century to study chemical dynamics.[2, 35-42] Advances in molecular beam scattering

techniques have allowed for the elucidation of the dynamics and mechanistic details of several classes of chemical reactions. The major challenge of performing molecular beam scattering techniques on the gas–liquid interface is that the liquid must be compatible with a vacuum environment. The original molecular beam experiments performed to probe the gas–liquid interface were done with a wetted wheel which allowed for the study of liquids with vapor pressures below $10^{-3}$ Torr.[43-47] The wetted wheel technique consists of a wheel rotating in a liquid reservoir to consistently replenish the liquid surface and is shown in Fig 1.2.3.

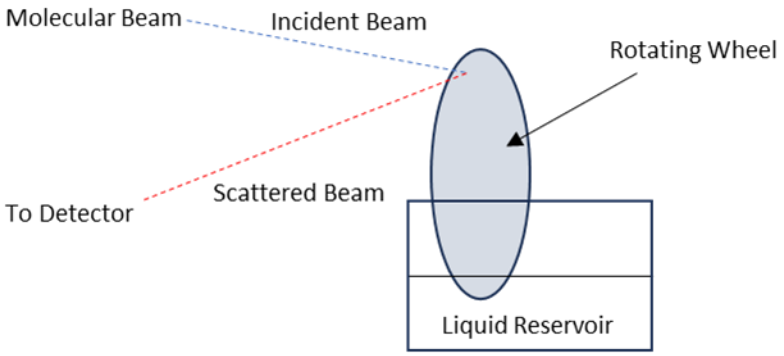


**Figure 1.2.3.** A schematic of the wetted wheel scattering technique. A rotating wheel is placed in a liquid reservoir to constantly replenish the liquid scattering surface. A molecular beam scatters gas molecules from the liquid surface of the wheel, the scattered particles are detected.

# 1.4 Liquid Jet Scattering

More volatile liquids have been studied largely through the efforts of Faubel and co-workers who developed a liquid microjet which allows for these liquids to be vacuum compatible.[48, 49] A schematic of liquid jet scattering is shown in Fig. 1.5.1 a. While liquid microjets allow for the study of a larger array of liquids than the wetted wheel, they pose specific problems when attempting molecular beam scattering experiments. First, they provide poor signal-to-noise ratios due to the relatively small diameter of the jet. Second, the cylindrical nature of a typical microjet does not allow for angularly-resolved scattering measurements.[34] Taking these considerations into account, our group incorporated a flat liquid jet into molecular beam scattering experiments using a microfluidic chip. The flat liquid jet is formed by colliding two cylindrical microjets to form a flat surface, a schematic of which is shown in Fig 1.5.1 b. Forming a flat jet provides a much larger scattering target (~1 mm). This simultaneously solves the issues of low signal-to-noise ratios and loss of angular specificity.

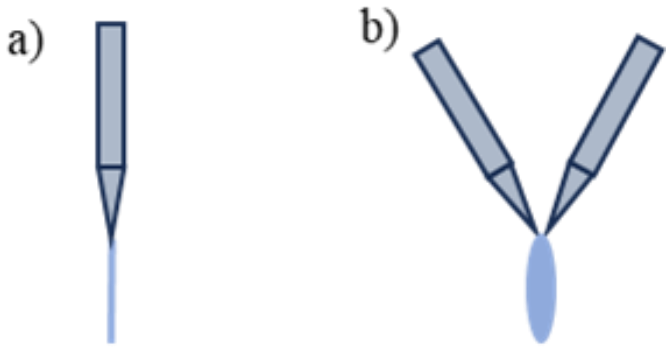


**Figure 1.5.1** a) Representation of a liquid microjet, the liquid jet diameter is ~25 μm on average. b) Representation of a flat liquid jet. Colliding two liquid microjets creates a flat sheet of liquid with a diameter of ~1 mm at its widest point.

The development of the flat liquid jet motivated two recent studies by our research group where Ne, $CD_4$, and $D_2O$ were scattered from dodecane.[50, 51] Dodecane was chosen as a target liquid specifically because of its relatively high vapor pressure ($1.5 \times 10^{-2}$ Torr at 275 K).[49] The choice of molecules to scatter from the dodecane jet followed from them all sharing a mass of 20 amu, but varying other physical properties, such as dipole moment, polarizability, and solubility. The liquid jet scattering work presented in this dissertation is a continuation of our previous work where the dynamics of $ND_3$ on a dodecane surface are investigated. This work can be found in chapter 6.

# 1.5 References

[1] M. E. Tuckerman, and G. J. Martyna, J. Phys. Chem. B **104** (2000) 159.
[2] D. Herschbach, Faraday Discussions of the Chemical Society **55** (1973) 233.
[3] D. R. Herschbach, Discussions of the Faraday Society **33** (1962) 149.
[4] Y.-T. Lee *et al.*, Review of Scientific Instruments **40** (1969) 1402.
[5] A. Rahman, Phys. Rev. **136** (1964) A405.
[6] T. G. Shepherd, Chem. Rev. **103** (2003) 4509.
[7] J. W. Morse, and D. Rickard, Environmental science & technology **38** (2004) 131A.
[8] J. N. Eisenberg, D. H. Bennett, and T. E. McKone, Environmental science & technology **32** (1998) 115.
[9] C. L. Brooks III *et al.*, PNAS **95** (1998) 11037.
[10] J. Ingham *et al.*, *Chemical engineering dynamics: an introduction to modelling and computer simulation* (John Wiley & Sons, 2008), Vol. 3,
[11] S. Y. van de Meerakker *et al.*, Chem. Rev. **112** (2012) 4828.
[12] J. Jankunas, and A. Osterwalder, Annu. Rev. Phys. Chem. **66** (2015) 241.
[13] M. L. Weichman, and D. M. Neumark, Annu. Rev. Phys. Chem. **69** (2018) 101.
[14] D. L. Osborn *et al.*, J. Chem. Phys. **106** (1997) 3049.
[15] E. N. Sullivan, B. Nichols, and D. M. Neumark, Phys. Chem. Chem. Phys. **21** (2019) 14270.
[16] A. Kunin, and D. M. Neumark, Phys. Chem. Chem. Phys. **21** (2019) 7239.

[17] R. Schinke, *Photodissociation dynamics: spectroscopy and fragmentation of small polyatomic molecules* (Cambridge university press, 1995), 1
[18] E. N. Sullivan, S. Saric, and D. M. Neumark, Phys. Chem. Chem. Phys. **22** (2020) 17738.
[19] A. J. Alexander, and R. N. Zare, Accts. Chem. Res. **33** (2000) 199.
[20] E. N. Sullivan, B. Nichols, and D. M. Neumark, J. Chem. Phys. **148** (2018)
[21] R. D. Levine, *Molecular reaction dynamics* (Cambridge University Press, 2009),
[22] E. N. Sullivan, in *Chemistry* (University of California, Berkeley, 2020).
[23] J. G. Anderson, Annu. Rev. Phys. Chem. **38** (1987) 489.
[24] H. Choi, R. T. Bise, and D. M. Neumark, J. Phys. Chem. A **104** (2000) 10112.
[25] B. Nichols *et al.*, J. Chem. Phys. **147** (2017)
[26] A. W. Harrison *et al.*, J. Chem. Phys. **145** (2016)
[27] B. Nichols, E. N. Sullivan, and D. M. Neumark, J. Chem. Phys. **152** (2020)
[28] A. Singh, and M. Agrawal, Journal of Environmental Biology **29** (2007) 15.
[29] R. Putikam, and M. C. Lin, Int. J. Quantum Chem. **118** (2018) e25560.
[30] M. F. Ruiz-Lopez *et al.*, J. Am. Chem. Soc. **141** (2019) 16564.
[31] D. Phillips, (University of East Anglia, 2022).
[32] M. E. Saecker *et al.*, Science **252** (1991) 1421.
[33] G. M. Nathanson, Annu Rev Phys Chem **55** (2004) 231.
[34] J. A. Faust, and G. M. Nathanson, Chem Soc Rev **45** (2016) 3609.
[35] D. Neumark *et al.*, The Journal of chemical physics **82** (1985) 3045.
[36] R. Continetti, B. Balko, and Y. T. Lee, The Journal of chemical physics **93** (1990) 5719.
[37] W. H. Weinberg, Advances in Colloid and Interface Science **4** (1975)
[38] J. Hurst *et al.*, Physical review letters **43** (1979) 1175.
[39] J. A. B. a. D. J. Auerbach, Surface Science **4** (1985)
[40] U. Harten *et al.*, Physical review letters **54** (1985) 2619.
[41] M. J. Cardillo, Surface Science (1994)
[42] Y. Huang *et al.*, Science **290** (2000) 111.
[43] M. E. King *et al.*, Physical review letters **70** (1993) 1026.
[44] P. D. Gilbert M. Nathanson, Douglas R. Worsnop, Charles E. Kolb, Journal of Physical Chemistry **100** (1996)
[45] J. Z. Bohan Wu, Timothy K. Minton, Kenneth G. McKendrick, John M. Slattery, Scott Yockel, George C. Schatz, Journal of Physical Chemistry **114** (2010)
[46] S. M. Brastad, and G. M. Nathanson, Phys. Chem. Chem. Phys. **13** (2011) 8284.
[47] P. D. Lane *et al.*, J. Phys. Chem. C **124** (2020) 16439.
[48] S. S. M. Faubel, and J.P. Toennies, Atoms, Molecules, and Clusters **10** (1988)
[49] M. Faubel, and T. Kisters, Nature **339** (1989) 527.
[50] C. Lee *et al.*, J Phys Chem A **126** (2022) 3373.
[51] W. Yang *et al.*, J Chem Phys **159** (2023)

# Chapter 2: Experimental Methods of Fast Beam Photofragment Spectroscopy

# 2.1 Experimental Scheme

Fast beam photofragment spectroscopy is an experimental technique used to study the photodissociation dynamics of free radical species. Although studying radical species is the primary goal of this technique, the reactive nature of free radicals makes them challenging to work with. The method used by our research group to create free radicals is to start with a stable precursor molecule which passes through an electric discharge creating an anion species. This anion is then subjected to a laser pulse providing it with enough energy to detach an electron, the product of this final reaction is the neutral free radical species we wish to study. The precursor reactions described are shown in equation 1.

Once the radical species is created, the photodissociation dynamics can be probed by subjecting the radical to another laser pulse initiating photodissociation, as shown in equation 2. The dissociation products are then detected and characterized to probe the dynamics of the photodissociation process.

$$Stable\ Precursor \xrightarrow{discharge} Anion \xrightarrow{h\nu_1} Neutral\ Radical \quad (1)$$

$$Neutral\ Radical \xrightarrow{h\nu_2} Dissociation\ Products \quad (2)$$

This process can be better visualized on a potential energy surface, one of which is shown in Fig 2.2.1. In most experiments, the anion species is given just enough energy by the first laser pulse to detach an electron and reach the ground vibrational state of the neutral radical, this is done by tuning the wavelength of the detachment dye laser to just above the electron affinity of the neutral. Once the neutral is created, the second laser pulse is used to excite the radical species and dissociation can take place. Fig 2.1 shows a repulsive potential energy surface which would result in an excited state dissociation process.[1] However, as mentioned in chapter 1, the excited state may also be a bound state which would result in a ground state dissociation process provided no predissociation takes place (see Fig 1.2.1).

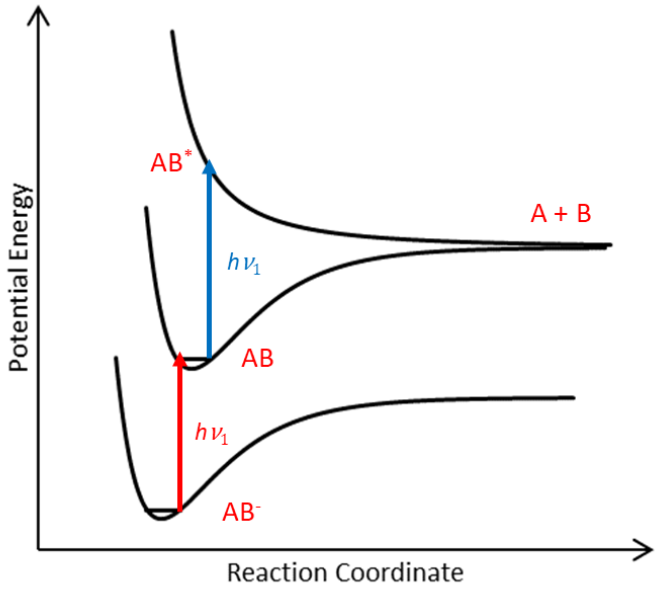


**Fig 2.1.** Relevant potential energy surfaces for anion $AB^-$ and neutral radical species AB during a fast beam photofragment dissociation experiment.

# 2.2 Fast Radical Beam Machine

## 2.2.1 Instrument Schematic

The fast radical beam machine (FRBM) is the instrument used to conduct fast beam photofragment dissociation experiments. FRBM was first constructed in the early 90's to study free radical photodissociation reactions, and has been modified several times over its long lifetime.[2, 3] A schematic of the FRBM instrument is shown in Fig 2.2. The remainder of this section serves as an ordered overview of the entire FRBM instrument.

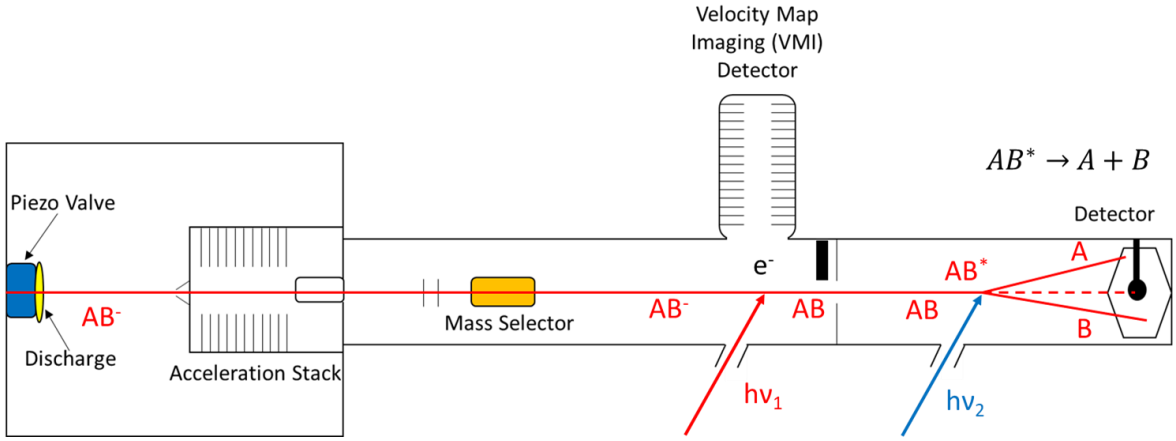


**Figure 2.2.1.** Schematic of the fast radical beam machine. The molecular beam path through the machine moves from left to right along the horizontal red line.

## 2.2.1 Amsterdam Piezo Valve

The molecular beam for this experiment is generated by an Amsterdam pulsed piezoelectric valve (MassSpecpecD BV, Enschede). [4, 5] The valve is backed by argon gas that is bubbled through the liquid precursor molecule of interest. The backing pressure of the valve is 30 psi, and it is pulsed at a repetition rate of 100 Hz. The valve is pulsed into high vacuum ~$10^{-6}$ torr creating a supersonic expansion which rapidly cools the molecules in the beam as they partition their internal energy into translational energy along the beam path.[6] The valve is operated with an opening time of ~30 μs with a repetition rate of 100 Hz.

## 2.2.2 Electric Discharge

After exiting the valve, the molecular beam enters the electric discharge where a constant direct current electric potential of ~ 2 kV is held between two pieces of stainless-steel mesh spaced 1 cm apart.[7] To maximize signal, the electric potential of the discharge varies, but is always in the range of 1.5 – 2.5 kV. The strong electric field of the discharge causes the gas molecules to ionize and is the section of the instrument where the precursor molecule becomes an anion.

## 2.2.3 Accelerator and Potential Switch

The product fragments of photofragment dissociation are typically neutral species which have a low probability of detection, further exasperated by the coincidence detection scheme used in our experiment. For this reason, it is necessary to accelerate the gas molecules in order to improve the detection efficiency.[8] The acceleration stack of the FRBM instrument is comprised of 16 resistively coupled plates which are used to accelerate the ions through a potential of 8 kV. Once exiting the acceleration stack, the ions enter the potential switch which consists of a stainless-steel cylinder held at 8 kV and pulsed to ground while the ion packet moves through the cylinder. Switching the potential to ground eliminates the need to float the entire instrument at 8 kV and references the molecules to a ground potential.

### 2.2.4 Mass Selector

Upon exiting the potential switch, the ion packet reaches the mass selector where two 3 inch length plates are positioned parallel to the beam at opposite sides. One plate is held at + 30 V while the other plate is held at - 30 V, deflecting any anions passing through the region. When the molecule of interest passes through the plates, the + 30 V plate is pulsed to - 30 V allowing the ions of the proper mass to continue along the beam path.

### 2.2.5 First Interaction Region and VMI Detector

Once the ions are mass selected, they are met with a laser pulse in the first interaction region. The laser pulse is generated by a Nd-YAG (Litron) pumped dye laser (Radiant Dyes) running at 100 Hz repetition rate. The wavelengths used by the detachment laser in this work are 562 nm, 568 nm, and 601 nm. The anions absorb the light from the laser and an electron is detached forming the neutral free radical species of interest. Our instrument is equipped with a velocity map imaging (VMI) detector located above the first interaction region perpendicular to the molecular beam axis.[9] The VMI is used to detect the detached electrons and generate a photoelectron spectrum.

While our VMI stack can provide us with relatively good resolution as described by Sullivan in her 2020 thesis, the purpose of the VMI is to characterize the radical species and verify that the molecule observed is the correct species.[9]

### 2.2.6 Flipper and Second Interaction Region

The radicals continue down the beam path where they encounter the flipper which is a deflection plate that is pulsed between ground and 200 V. The purpose of the flipper is to deflect

any anions that were not photodetached in the first interaction region. This assures that only the free radicals of interest are in the molecular beam upon reaching the second interaction region.

In the second interaction region, the neutrals encounter a second laser pulse from an unpolarized excimer laser (GAM). The experiment originally featured a dye laser (LPX); however, the laser was switched to allow experiments with higher energy photons. Wavelengths used in this work are 248 nm and 193 nm. At this stage, one of the neutrals in the beam may absorb a photon and will have enough energy to dissociate. Dissociated fragments will spread out from the beam path and collide with the detector face. Undissociated radicals continue straight down the beam path and collide with the beam block placed in front of the detector. The beam block ensures that the detector is only detecting the fragments and not the radicals themselves.

### 2.27 Coincidence Detector

The photodissociation fragments are collected using a hexanode delay line detector (RoentDek). This detector has been well described in the past.[10] The hexanode delay line detector provides 2-dimensional position data as well as time data for each particle detected. Using the arrival time, position, and parent mass, the masses and translational energies of the fragments can be characterized. For our experiment, both two and three-body dissociation events are detected in coincidence.

## 2.3 Data Analysis

### 2.3.1 Two-Body Mass Distributions

One of the initial goals of FRBM experiments is to determine the dissociation channels and their relative branching ratios. The coincidence detector allows us to determine the masses of our fragments using conservation of momentum. The conservation of momentum dictates that in a center of mass coordinate system the momentum vectors must sum to 0.[11] This law is demonstrated by the two body case shown in equation 3.

$$m_1\vec{v}_1 + m_2\vec{v}_2 = 0 \qquad (3)$$

Substituting for the velocity vectors with displacement vectors from the beam center ($\vec{r}_1$, $\vec{r}_2$) and arrival times ($t_1$, $t_2$), then rearranging equation 3 leads to equation 4.

$$m_1 \frac{\vec{r}_1}{t_1} = -m_2 \frac{\vec{r}_2}{t_2} \quad (4)$$

Making the assumption that the arrival times of the fragments are equal, substituting for the magnitude of the displacement vectors, and rearranging leads to equation 5.

$$\frac{m_1}{m_2} = \frac{r_2}{r_1} \quad (5)$$

While the detector does not measure either of the fragment masses, the sum of the two masses must be the parent mass M as shown in equation 6. This parent mass can then be substituted into equation 5 to yield equation 6.

$$M = m_1 + m_2 \quad (6)$$

$$\frac{M - m_2}{m_2} = \frac{r_2}{r_1} \quad (7)$$

Equation 8, which gives the mass of fragment 2 in terms of the position vectors of the two fragments and the parent mass is obtained through a simple algebraic rearrangement of equation 7.

$$m_2 = \frac{M}{1 + \frac{r_2}{r_1}} \quad (8)$$

From equation 8 The mass of one of the fragments can be found and the other mass is calculated using equation 6. Once the masses are found, they are plotted in a 2-body mass diagram. Fig 2.3.1 provides a sample 2-body mass diagram for the species iso-propoxyl.[12]

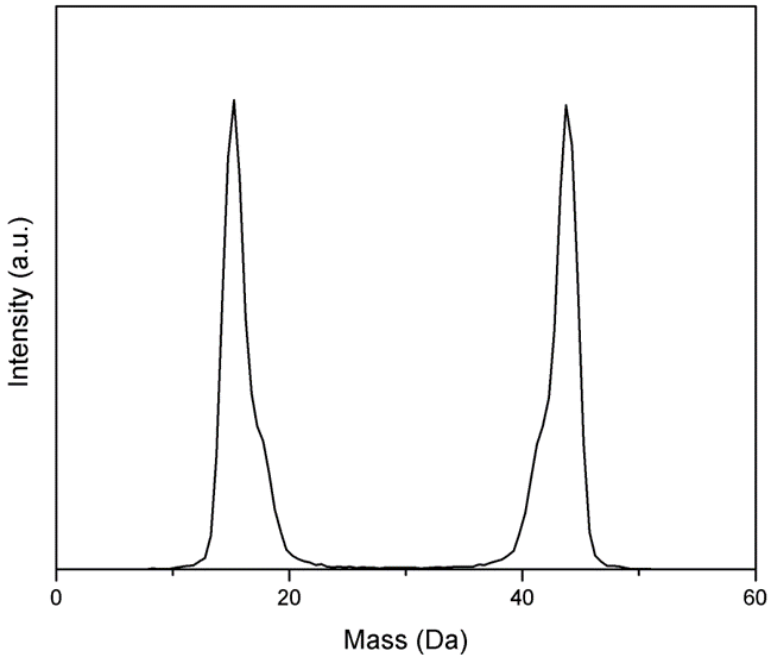


**Figure 2.3.1.** Example two-body mass distribution for iso-propoxy shows two distinct peaks at masses 15 and 44 amu assigned to $CH_3$ and $CH_3CHO$, and shoulder peaks at 17 and 42 amu assigned to OH and $C_3H_6$.[12]

Due to our coincidence detection scheme, 2-body mass distributions will always appear symmetric, centered at one half of the parent mass. From the distribution, channel assignments are made, and branching ratios can be calculated from the number of counts in each channel.

## 2.3.2 Three-Body Mass Distributions

The coincidence detector has the capability to detect three particles in coincidence, which can be used to construct 3-body mass distributions. An analysis similar to the one performed for 2-body mass distributions can be performed for 3-body mass distributions according to the conservation of momentum shown in equation 9.

$$m_1\vec{v}_1 + m_2\vec{v}_2 + m_3\vec{v}_3 = 0 \qquad (9)$$

The details of solving for the three fragment masses is nearly identical to the analysis performed for 2-body mass distributions in section 2.3.1, with the exception that there are now three variables to solve for and only two equations, so one must be assigned. The choice of assignment is the assignment which minimizes the deviation between the center of mass and center of the

neutral beam.[9] Since there is some ambiguity in the choice of assignment, this can lead to false assignments of particular coincident events. These false coincidences have been well described in the past and must be accounted for when assigning dissociation channels to three body mass distributions.[9] Fig. 2.3.2 shows a sample 3-body mass distribution for the radical iso-propoxyl.[12]

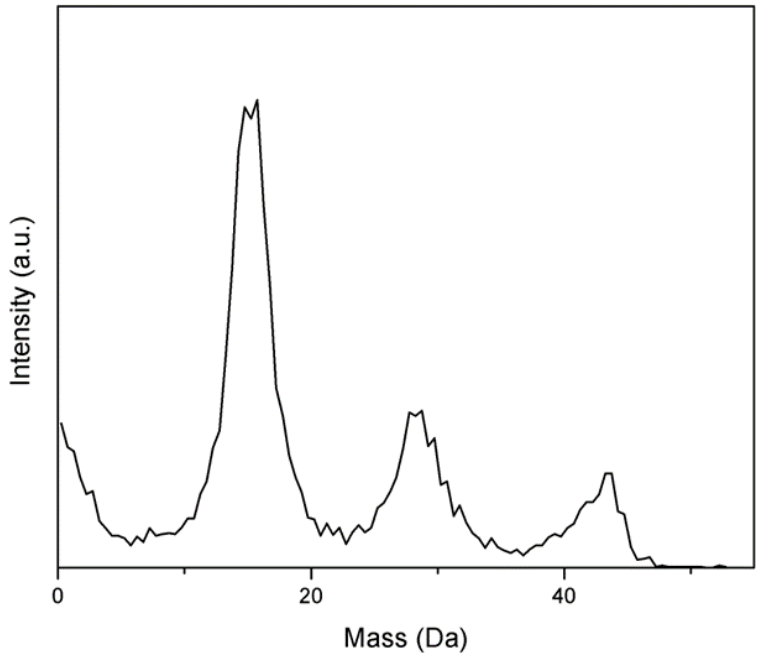


**Figure 2.3.2.** Example 3-body mass distribution for the radical species iso-propoxyl showing peaks corresponding to 3 different dissociation channels, $CH_4$, $CH_3$, and CO, $CH_3$, $CH_3$, and HCO, and H, $CH_3$, and $C_2H_3O$.

Note that for 3-body mass distributions, the peak symmetry that was seen in 2-body distributions is broken. Also, if there is overlap between masses from different channels, the intensity of some peaks become larger than others from the same coincident event.

Once a 3-body mass distribution is constructed, dissociation channels are assigned while taking into account peak overlap, peak intensity, and the possibility of false coincidences. From this point, branching ratios are also assigned.

## 2.3.3 Translational Energy Distributions

In addition to position information, the coincidence detector also records arrival times for each particle. The arrival times can be used to calculate the velocity of each particle by considering the distance between particle positions. The translational energy of the coincident

particles are summed for each coincident event and plotted as a distribution separately for each dissociation channel assignment. An example translational energy distribution for a 2-body channel of iso-propoxyl is given in Fig 2.3.3.[12]

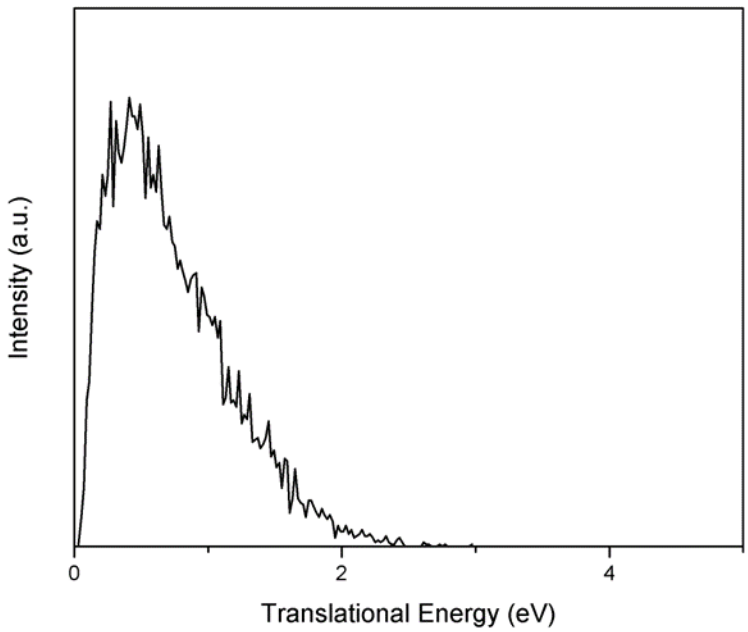


**Figure 2.3.3.** Example translational energy distribution for the OH and $C_3H_6$ 2-body dissociation channel of iso-propoxy at 248 nm.

Constructing translational energy distributions allows for the main goal of fast beam photofragment spectroscopy which is to characterize the dissociation mechanism for each channel of the radical species of interest. This characterization is generally performed by comparing the peak of the translational energy distribution to the maximum available translational energy imparted by the dissociation photon. The relevant equation to find the maximum possible translational energy $E_{\mathrm{T,max}}$ is given by equation 10.

$$E_{\mathrm{T,max}} = h\nu_2 - D_0 \qquad (10)$$

Here $h\nu_2$ is the energy of the dissociation photon and $D_0$ is the dissociation energy of that channel. The energy of the photon is given by the wavelength of light output by the dissociation laser, while the dissociation energy of the channel is calculated using the enthalpy of formation for the products and reactants. Experimental values for the enthalpy of formation are used when available but must be calculated theoretically using ab initio quantum chemistry software if they

are not. In the past, the $E_{\mathrm{T,max}}$ has been identified for excited state dissociation, and used to calculate $D_0$.[13]

Comparing $E_{\mathrm{T,max}}$ to the peak of the translational energy diagrams can be used to determine whether dissociation for that channel occurred on the ground state or excited state. If dissociation occurs on an excited state, a repulsive potential causes the majority of the available energy to be partitioned into translation along the reaction coordinate and $E_T \approx E_{\mathrm{T,max}}$. Conversely, if dissociation occurs on a ground state, energy must be partitioned into the internal degrees of freedom of the molecule to undergo internal conversion to the ground state before dissociation can take place and $E_T \ll E_{\mathrm{T,max}}$.

### 2.3.4 Analysis Software

The photoelectron spectra are simulated using calculation from the quantum chemistry software Gaussian, and the photoelectron spectra simulation software ezFCF.[14, 15]. The FRBM data analysis software responsible for construction of mass distributions and translational energy distributions is FRBM_Analysis. FRBM_Analysis was written in C++ and is contained in its entirety in the thesis of Alexandra Hoops, while all modifications to the original software are listed in the thesis of Erin Sullivan.[9, 16]

## 2.4 References

[1] A. J. Alexander, and R. N. Zare, Accts. Chem. Res. **33** (2000) 199.
[2] R. Continetti *et al.*, Chemical physics letters **182** (1991) 406.
[3] A. W. Harrison *et al.*, J. Chem. Phys. **145** (2016)
[4] D. Irimia *et al.*, Review of Scientific Instruments **80** (2009)
[5] C. Meng, and M. H. Janssen, Review of Scientific Instruments **86** (2015)
[6] M. D. Morse, Experimental methods in the physical sciences **29** (1996) 21.
[7] E. Garand, T. I. Yacovitch, and D. M. Neumark, J. Chem. Phys. **130** (2009)
[8] S. Hosokawa *et al.*, Rev. Sci. Instrum. **81** (2010)
[9] E. N. Sullivan, in *Chemistry* (University of California, Berkeley, 2020).
[10] A. W. Harrison, (University of California – Berkeley, 2014).
[11] J. R. Taylor, and J. R. Taylor, *Classical mechanics* (Springer, 2005), Vol. 1,
[12] E. N. Sullivan, S. Saric, and D. M. Neumark, Phys. Chem. Chem. Phys. **22** (2020) 17738.
[13] D. L. Osborn *et al.*, Chemical Physics Letters **235** (1995) 484.
[14] M. J. Frisch *et al.*, Wallingford, CT, 2016).
[15] A. I. K. S. Gozem, P. Wojcik, S. Gozem, V. Mozhayskiy, in *The ezSpectra suite: An easy-to-use toolkit for spectroscopy modeling* ( WIRES CMS, 2021).
[16] A. A. Hoops, in *Chemistry* (U.C. Berkeley.

# Chapter 3: Photodissociation of the Methyl Phenoxy Radical at 193 nm

# 3.1 Introduction

Molecular dynamics is a field interested in the study of the microscopic movements and energy partitioning of molecules.[1] Both experimental and theoretical techniques to probe the dynamics of molecules and chemical reactions have been developed since the early 1960's.[2-5] These techniques have led to unprecedented levels of detail in the fundamental understanding of both reactive and non-reactive molecular motion which has played a significant role in countless fields including atmospheric chemistry, environmental science, biochemistry, and chemical engineering.[1, 6-10]

The development of molecular beam experiments in particular has been important to the understanding of molecular dynamics in a wide variety of fields.[11, 12] For more than thirty years, our research group has made use of various molecular beam experiments to study the molecular dynamics of many systems relevant in physics, chemistry, and biology.[13-16] The work performed in this chapter attempts to investigate the photodissociation dynamics of the methyl phenoxy radical.

The methyl phenoxy radical is a free radical formed from the hydrogen abstraction of the common organic solvent cresol. Cresols are naturally occurring by products of biochemical reactions, but are often produced during the manufacturing of organic solvents.[17] The biggest source of cresols in the environment is through the burning of wood and fossil fuels in which cresol is released into the atmosphere and broken down naturally over the course of 1 to 2 days.[17] Cresols and most of their related products including methyl phenoxy have three different isotopes, meta, ortho, and para as shown in Fig. 3.1.1.

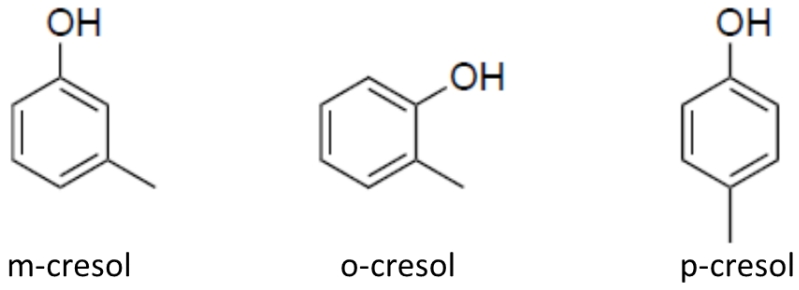


**Figure 3.1.1.** Structures of m-cresol (meta), o-cresol (ortho), and p-cresol (para).

The methyl phenoxy radical is one of the potential products formed from the decomposition of cresol, as well as from other cresol products such as methyl phenol ether.[18, 19] While the phenoxy radical has been studied extensively, very little work has been done investigating the properties of methyl phenoxy radicals.[15, 20-24] Mechanisms involving the oxidation of cresol to form methyl phenoxy radicals were studied in the aqueous phase in 2006.[25]

Shortly after, density functional theory was used to determine the difference in enthalpies of formation between the methyl cresol radicals and their cresol radical counterparts in 2007.[26]. More recently, Lineberger measured the electron affinities of the three methyl phenoxy radicals using anion photoelectron spectroscopy in 2017.[27] The electron affinities measured from this work are 2.22, 2.20, and 2.12 eV for the meta, ortho, and para methyl phenoxy radicals respectively.[27]

This work will investigate the photodissociation dynamics of the methyl phenoxy radical using fast beam photofragment spectroscopy. The relevant two and three-body dissociation channels of the methyl phenoxy radical and their dissociation energies are shown in Fig 3.1.2. Dissociation energies are calculated from the heats of formation of each species. Heats of formation for the product species are all taken from Tsang or Chase.[28, 29] Heats of formation for the methyl phenoxy radicals were calculated to be 2.12, 1.01, and 0.83 eV for the meta, ortho, and para isomers respectively. Calculated values were obtained from density functional theory with the B3LYP functional and 6 31G basis set using the ab initio quantum chemistry software Gaussian.[30]

| | | |
|---|---|---|
| Channel 1: | $CH_3C_6H_4O \rightarrow HCO + C_6H_6$ | $D_0 = -0.82, 0.30, 0.48$ eV |
| Channel 2: | $CH_3C_6H_4O \rightarrow H + CO + C_6H_6$ | $D_0 = -0.21, 0.91, 1.09\ eV$ |
| Channel 3: | $CH_3C_6H_4O \rightarrow CO + C_2H_3 + C_4H_4$ | $D_0 = 2.83, 4.13, 3.94\ eV$ |
| Channel 4: | $CH_3C_6H_4O \rightarrow HCO + C_3H_3 + C_3H_3$ | $D_0 = 5.35, 6.47, 6.65\ eV$ |

**Figure 3.1.2.** The relevant two and three-body dissociation channels of the methyl phenoxy radical at 193 nm. The dissociation energies of each reaction have three different values corresponding to the three isomers of methyl phenoxy: meta, ortho, and para respectively. All dissociation energies are calculated from heats of formation of the individual species. Heats of formation of the product species are taken from Tsang or Chase.[28, 29] The heats of formation for the methyl phenoxy radicals were calculated using density functional theory with a B3LYP functional and 6 31G basis set from the quantum chemical software Gaussian.[30] Values of 2.12, 1.01, and 0.83 eV were calculated for the meta, ortho, and para methyl phenoxy radicals respectively.

# 3.2 Experimental Methods

The photodissociation dynamics of the methyl phenoxy radical is investigated using fast beam photofragment spectroscopy. The instrument used to perform these experiments is the fast radical beam machine (FRBM) described in detail in Chapter 2 Section 2 of this dissertation. The formation of methyl phenoxy anions in the molecular beam was originally discovered by accident. Toluene was placed in the bubbler and a backing gas comprised of 98 % argon and 2 %

fluorine was pressurized to 30 psi in the Amsterdam piezo valve. After entering the chamber of the FRBM, and passing through the electric discharge, it was discovered through mass selection and photoelectron spectroscopy that the anion species in our beam was indeed methyl phenoxy. This curious process to form methyl phenoxy is shown in Fig. 3.2.1. Perhaps the most surprising thing about this reaction is that the source of the oxygen on methyl phenoxy is unknown. Some speculation in our research group has suggested that it may come from the formation of oxidized compounds on the electric discharge grids, atmospheric oxygen entering the gas mixture through small leaks in the valve manifold, or trace amounts of water that has contaminated the toluene in the bubbler. Although these are the most likely candidates, none of these explanations seem very plausible or would account for the relatively large amount of anion signal seen in the molecular beam.

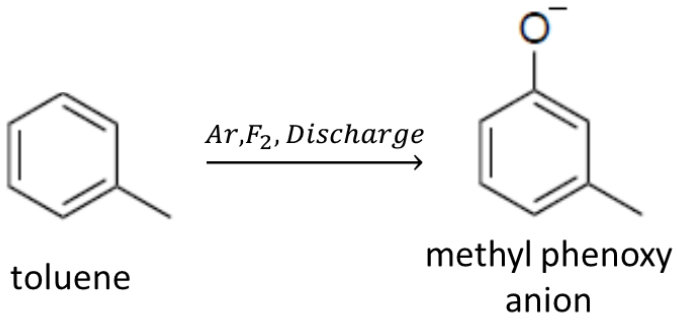


**Figure 3.2.1.** The electric discharge reaction with toluene to form the methyl phenoxy anion. The source of the oxygen in this reaction is not known. Only the meta isomer is shown, but all three isomers are formed.

The methyl phenoxy anions in the molecular beam are mass selected and photodetached in the first interaction region to form the methyl phenoxy radical according to Figure 3.2.2. The laser pulse used for photodetachement is generated by a frequency doubled Nd-YAG (Litron) laser producing photons at 532 nm (2.33 eV). The electrons detached in this process are collected to generate a photoelectron spectrum and identify the methyl phenoxy radical.

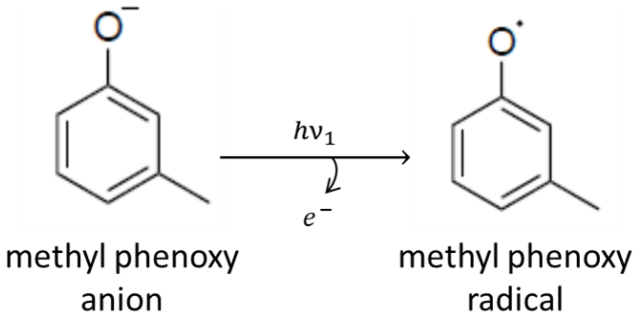


**Figure 3.2.2.** Formation of methyl phenoxy radical from methyl phenoxy anion using a 532 nm photon from the detachment laser of the FRBM. Only the meta isomer is shown, but all three isomers are formed.

The methyl phenoxy radicals are allowed to continue to the second interaction region where they are subjected to a second laser pulse from a 193 nm (6.42 eV) ArF excimer laser. The energy of this laser pulse was chosen as a first look at this species, in which we typically use the highest energy photons available for photodissociation. The excited methyl phenoxy radicals initiate photodissociation and the products are detected on a hexanode delay line detector (RoentDek).

# 3.3 Results and Discussion

## 3.3.1 Photoelectron Spectrum

The photoelectron spectrum for the methyl phenoxy radical at 532 nm is shown in figure 3.3.1. The stationary states of the three isotopes of methyl phenoxy (meta, ortho, and para) are calculated using the ab initio quantum chemistry software Gaussian and the photoelectron spectra are simulated using the software ezFCF.[30, 31] Peak assignments of the photoelectron spectrum are made using the assignments provided by Lineberger.[27] The major peaks of our spectrum match well with the peaks of our three simulated isomers, suggesting that methyl phenoxy radicals are the identity of the neutral species in our molecular beam. Our group was unable to isolate a single isomer, and photodissociation was conducted on the mixture of all three isomers present in the molecular beam.

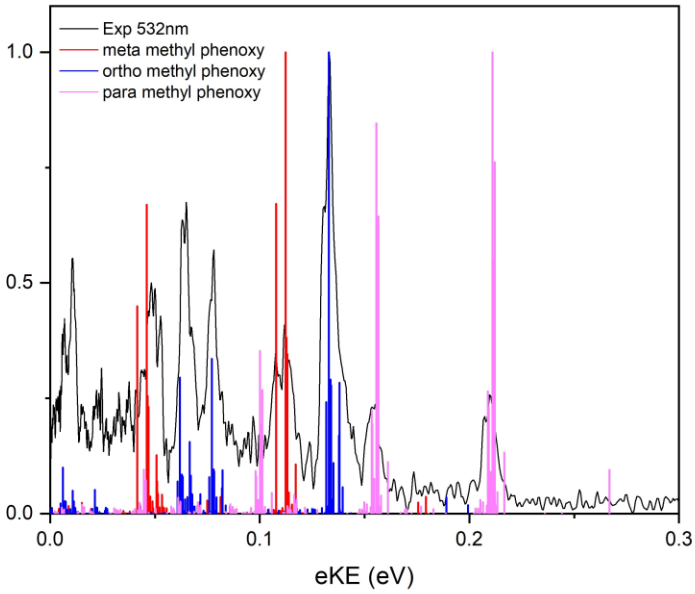


**Figure 3.3.1.** Photoelectron spectrum of the methyl phenoxy anion at 532 nm. The experimental spectrum is a mixture of all three isomers of methyl phenoxy. The simulated spectra for the meta, ortho, and para isomers are plotted in red, blue, and pink respectively. The simulated spectra account for all major peaks in the experimental spectrum suggesting that the identity of the species present is indeed methyl phenoxy.

## 3.3.2 2-Body Mass Distribution

Photodissociation of the methyl phenoxy radical was conducted at 193 nm (6.42 eV) and the product fragments were detected in coincidence. The 2-body mass distribution for the photodissociation of the methyl phenoxy radical is shown in Fig 3.3.2. The 2-body mass distribution for methyl phenoxy only consists of 2 peaks, one at 29 amu and 78 amu. Since the detector collects particles in coincidence, these peaks represent a single 2-body dissociation channel for the methyl phenoxy radical.

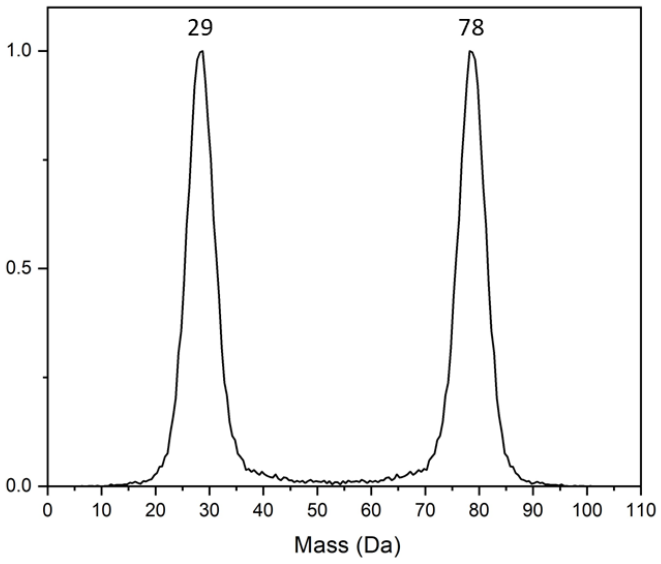


**Figure 3.3.2.** The 2-body mass distribution of methyl phenoxy photodissociation at 193 nm (6.42 eV). The distribution contains only 2 peaks at masses of 29 amu and 78 amu.

The assignment given to the 2-body photodissociation of the methyl phenoxy radical is the formyl radical for the peak at 29 amu and benzene for the peak at 78 amu, this channel labeled channel 1 is shown in figure 3.3.3. The 2-body channel assignment for the peaks at 29 amu and 78 amu is fairly easy to assign, because only one pair of species that's known to exist have these fragment masses and the correct molecular formulas to react and form a methyl phenoxy radical.

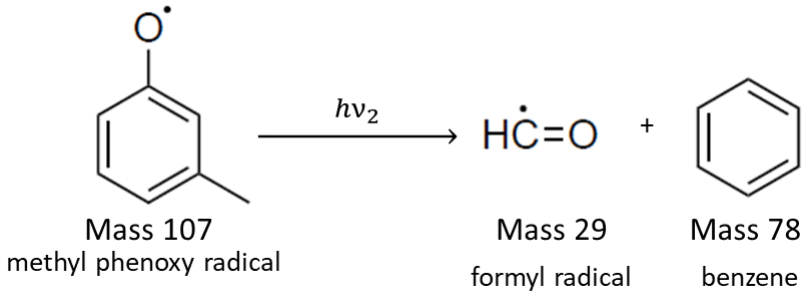


**Figure 3.3.3.** Channel 1 of the photodissociation of the methyl phenoxy radical at 193 nm. The only 2-body channel consists of dissociation of the methyl phenoxy radical to form a formyl radical and benzene. Only the meta isomer is shown, but all three isomers can dissociate via this channel.

### 3.3.3 3-Body Mass Distribution

The 3-body mass distribution of the photodissociation of the methyl phenoxy radical at 193 nm is shown in Fig 3.3.4. In contrast to the 2-body distribution, the 3-body distribution has more than one dissociation channel present and several more peaks present in the distribution. Peaks appear at 1, 28, 39, 52, and 78 amu with a potential shoulder in the 28 amu peak at 27 amu. The peak at 28 amu is particularly strong with about 3 times the intensity of the other peaks in the distribution.

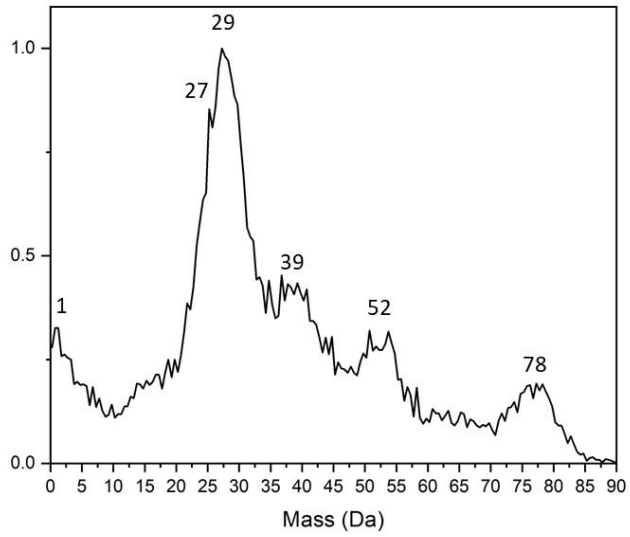


**Figure 3.3.4.** The 3-body mass distribution for the photodissociation of the methyl phenoxy radical at 193 nm. The distribution contains peaks at 1 amu, 28 amu, 39 amu, 52 amu, and 78 amu with a potential shoulder at 27 amu.

Assignment of the channels is slightly more difficult for the 3-body distribution, but in several cases can be determined by the process of elimination and the energetics of the existing chemical species. The first and most obvious assignment is channel 2 which consists of the peak at 1 amu being assigned to hydrogen, the peak at 28 amu being assigned to carbon monoxide, and the peak at 78 amu being assigned to benzene. Channel 2 is shown in Fig. 3.3.5.

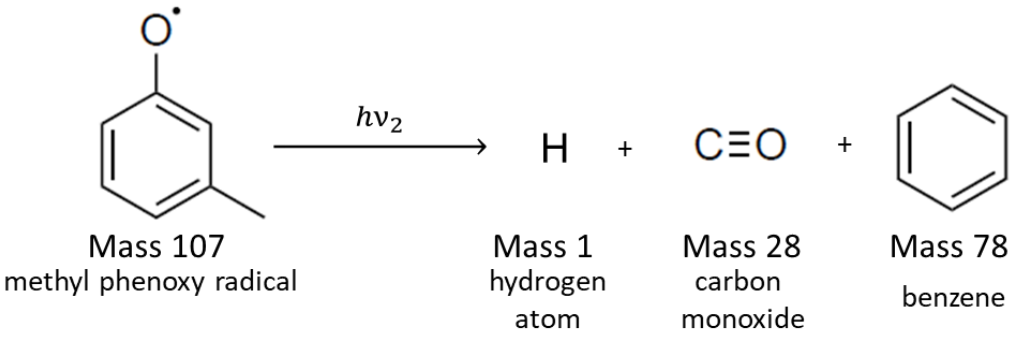


**Figure 3.3.5.** Channel 2 of the photodissociation of the methyl phenoxy radical at 193 nm. Channel 2 consists of a hydrogen atom at mass 1, carbon monoxide at mass 28, and benzene at mass 78 for the dissociation fragments of the methyl phenoxy radical. Only the meta isomer is shown, but all three isomers can dissociate via this channel.

Channel 2 was the most obvious 3-body assignment because its products are very similar to the products seen in channel 1. The dissociation products of channel 1 are benzene and the formyl radical, while the dissociation products of channel 2 are benzene, carbon monoxide and hydrogen. It is highly likely that channel 2 is a sequential dissociation event where the methyl phenoxy radical dissociates to benzene and a formyl radical as expected, but enough energy is imparted to the formyl radical to further dissociate into carbon monoxide and a hydrogen atom. The required energy for the dissociation of HCO to H and CO is 0.6 eV, making it highly likely for this process to occur with ~6 eV of energy leftover in the product fragments. For this reason, it is reasonable to consider channel 2 to be a secondary dissociation following the original 2-body dissociation of channel 1.

It is important to note that 0.6 eV being imparted to the formyl radical should be a very common occurrence, and it is possible that channel 1 does not exist at a dissociation energy of 6.42 eV. Meaning all channel 1 coincident events are channel 3 coincident events where the hydrogen is not detected. While there is a strong possibility that this is the case, without further experiments it would be difficult to prove, and under these circumstances, we will operate under the assumption that two body dissociation events are channel 1 dissociation events.

Accounting for the three times intensity of the peak at 28 amu and the accompanying shoulder at 27 amu, channel 3 follows as the next logical assignment. Channel 3 consists of the peak at 28 amu being assigned to carbon monoxide, the shoulder at 27 amu being assigned to the vinyl radical, and the peak at 52 amu being assigned to 1-buten-3-yne. Channel 3 is shown in Fig 3.3.6.

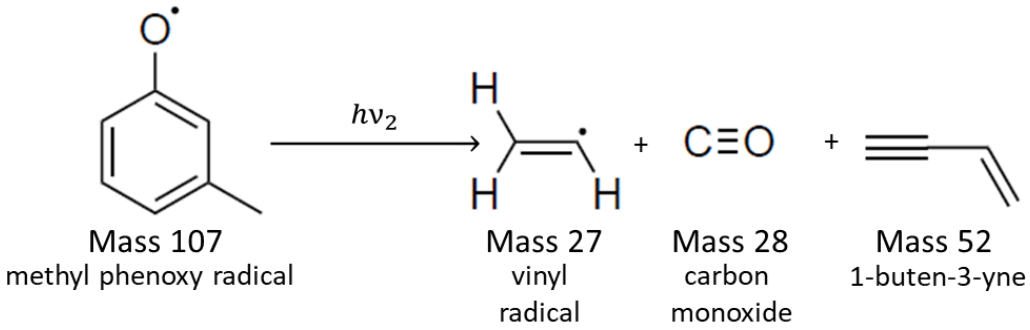


**Figure 3.3.6.** Channel 3 of the photodissociation of the methyl phenoxy radical at 193 nm. Channel 3 consists of the vinyl radical at mass 27, carbon monoxide at mass 28, and 1-buten-3-yne at mass 52 amu dissociating from the methyl phenoxy radical. Only the meta isomer is shown, but all three isomers can dissociate via this channel.

The assignments of channels 2 and 3 account for all peaks seen in the 3-body mass distribution apart from the peak at mass 39 amu. This peak is most likely assigned to the propargyl radical. For the assignment of this peak to work properly, the dissociation products would need to be two propargyl radicals at mass 39 amu, and a formyl radical at mass 29 amu which is labeled channel 4 and shown in Fig. 3.3.7. Similar to channel 2, channel 4 is likely a sequential dissociation process following channel 1. In this case, the methyl phenoxy radical will dissociate to a formyl radical and benzene via channel 1; however, if enough energy is imparted to the benzene fragment it will further dissociate to two propargyl radicals via channel 4. The energy required for the further dissociation of benzene to two propargyl radicals is 6.17 eV which is greater than the maximum energy available for the ortho and para isomers, so only the meta isomer would be expected to proceed via channel 4.

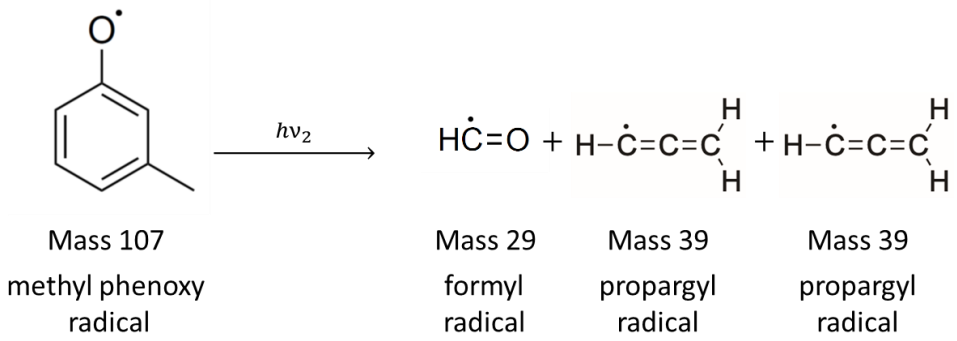


**Figure 3.3.7.** Channel 4 of the photodissociation of the methyl phenoxy radical at 193 nm. Channel 4 consists of the formyl radical at mass 29 amu and two propargyl radicals at mass 39 amu dissociating from the methyl phenoxy radical. Only the meta isomer is shown, but all three isomers may dissociate via this channel.

### 3.3.4 Branching Ratios

The photodissociation of the methyl phenoxy radical at 193 nm results in 4 channels. The only 2-body dissociation channel, channel 1 consists of a formyl radical and benzene which accounts for 83 % of total dissociation events. The three 3-body channels make up the remaining 17 % of total dissociation events. Channel 2, which is likely a sequential dissociation mechanism following channel 1 accounts for 4 % of total dissociation events and dissociates into a hydrogen atom, carbon monoxide and benzene. Channel 3 which consists of the dissociation fragments, carbon monoxide, 1-buten-3-yne, and the vinyl radical accounts for 7 % of total dissociation events. Channel 4 corresponds to the dissociation fragments of 2 propargyl radicals and a formyl radical and accounts for 5 % of total dissociation events. The 3-body channels 2 and 4 are suspected of being sequential dissociation events following channel 1, in which 0.6 eV partitioned into the formyl radical may result in further dissociation to hydrogen and carbon dioxide via channel 2, or 6.17 eV partitioned into the benzene may result in dissociation to two propargyl radicals via channel 4. If channels 2 and 4 represent sequential dissociation mechanisms, then 93 % of initial dissociation proceeds via channel 1 at 193 nm.

### 3.3.5 Translational Energy Distributions

As mentioned previously, the translational energy distributions for each dissociation channel are measured and can be used to characterize the dissociation mechanism for each channel. The translational energy distribution for channel 1 is shown in Fig 3.3.8. The red text on the plot indicates the maximum available translational energy. The dissociation energies of channel 1 for the three isomers of the methyl phenoxy radical are -0.81, 0.30, and 0.48 eV for the meta, ortho, and para isomers respectively.[28, 32] At a photon energy of 6.42 eV (193 nm) these dissociation energies correspond to maximum translational energies $E_{\mathrm{T,max}}$ of 7.2, 6.1, and 5.9 eV for meta, ortho, and para respectively. The translational energy distribution for channel 1 peaks around 0.6 eV meaning that in the case of channel 1 $E_{\mathrm{T}} \ll E_{\mathrm{T,max}}$ which is indicative of internal conversion to the ground state followed by statistical dissociation.

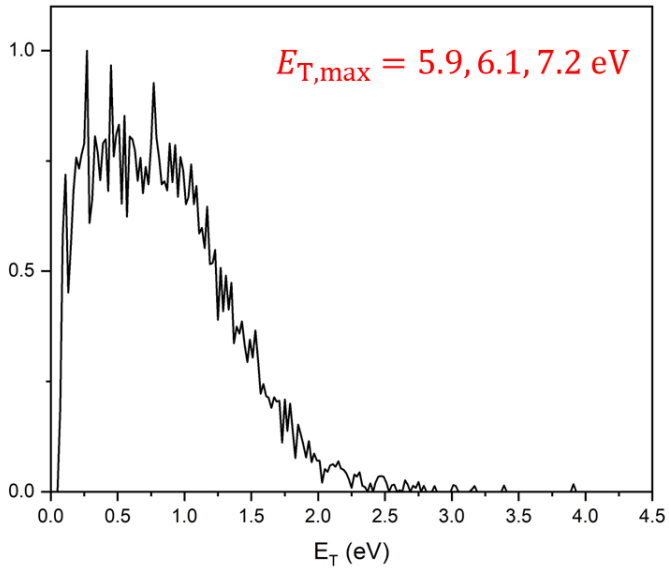


**Figure 3.3.8.** The translation energy distribution for channel 1 of the photodissociation of the methyl phenoxy radical at 6.42 eV. The maximum translational energies of the three methyl phenoxy radicals are 7.2, 6.1, and 5.9 eV for the meta, ortho, and para isomers respectively.

Channel 2 corresponds to the dissociation of the methyl phenoxy radical to a hydrogen atom, carbon monoxide, and benzene. The dissociation energies for this channel are -0.21, 0.91, and 1.09 eV for the meta, ortho, and para isomers of the methyl phenoxy radical respectively.[28, 32] These dissociation energies correspond to $E_{T,max}$ values of 6.6, 5.5, and 5.3 eV for the meta, ortho, and para isomers respectively with a dissociation photon energy of 6.42 eV. Similar to channel 1, there is a lot of excess energy available for excitation of the fragments. The translational energy distribution for dissociation channel 2 of the methyl phenoxy radical is shown in figure 3.3.9. The translational energy distribution for channel 2 peaks around 1.0 eV which means that $E_T \ll E_{T,max}$ and once again indicative of internal conversion to the ground state followed by statistical dissociation.

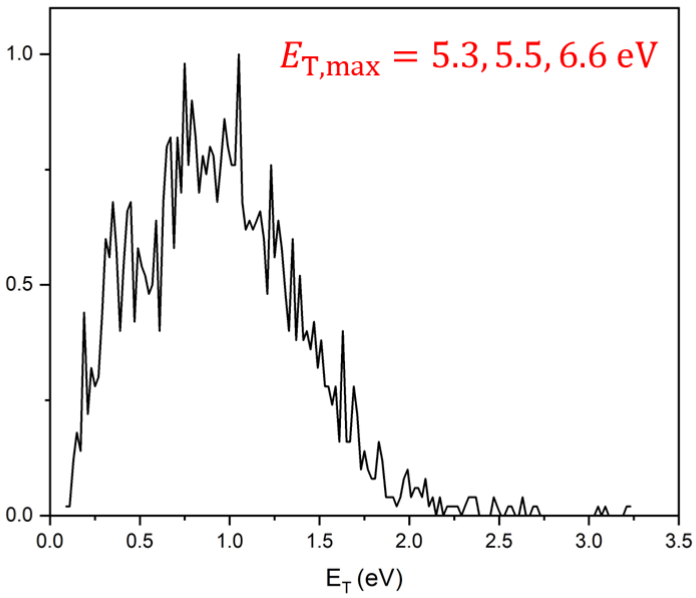


**Figure 3.3.9.** The translational energy distribution of dissociation channel 2 of the methyl phenoxy radical at 6.42 eV. The maximum translational energies for the meta, ortho, and para isomers of the methyl phenoxy radical are 6.6, 5.5, and 5.3 eV respectively.

The dissociation energy difference between channel 1 and channel 2 corresponds to an energy of 0.61 eV which is the dissociation energy of the formyl radical to a hydrogen atom and carbon monoxide. For channel 2 to correspond to a sequential mechanism of channel 1, at least 0.61 eV of energy must be partitioned into the formyl radical fragment. Since benzene contains many more internal degrees of freedom than a formyl radical, statistically it will contain much more energy than the formyl radical in most cases. This means that most channel 1 dissociation pairs partition the majority of their energy into the internal degrees of freedom of benzene and will have a lower total translational energy. However, for a channel 1 dissociation pair that contains more energy in the formyl radical, we would expect to see a higher percentage of that energy partition into translation. Meaning that the higher translational energy peak for channel 2 over channel 1 is strong evidence in support of channel 2 as a sequential dissociation mechanism of channel 1.

The dissociation energies for channel 3 are 2.8, 3.9, and 4.1 eV for the meta, ortho, and para isomers of the methyl phenoxy radical respectively.[28, 32] These dissociation energies correspond to maximum translational energies of 3.6, 2.5, and 2.3 eV for the meta, ortho, and para isomers respectively. The translational energy distribution for dissociation channel 3 of the methyl phenoxy radical is shown in Fig. 3.3.10. The translational energy of the channel 3 fragments peaks around 1.25 eV, and the maximum translational energy of the para-methyl

phenoxy radical is 2.8 eV. While the translational energy of channel 3 is much closer to the maximum, it still differs by more than 1.5 eV and is most likely indicative of a ground state dissociation process. It is important to note that the translational energy distribution extends slightly past the maxima for the para and ortho isomers. These higher energy pairs above energies of 2.5 eV likely come from the meta isomer and not the other two. The dissociation mechanism for this channel would need to be much more complicated than those of channels 1 and 2 and involve substantial isomerization to take place. Since isomerization generally requires significant partitioning of energy into internal degrees of freedom, this makes a ground state dissociation process more likely for channel 3.

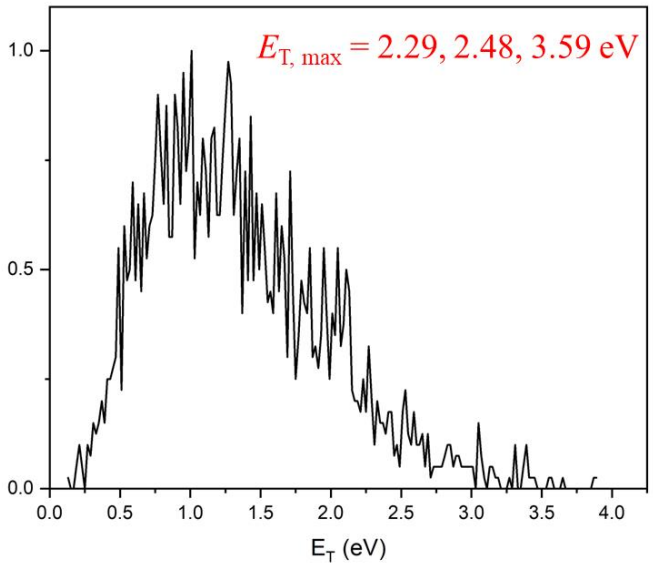


**Figure 3.3.10.** The translational energy distribution of dissociation channel 3 of the methyl phenoxy radical at 6.42 eV. The maximum translational energies for the meta, ortho, and para isomers of the methyl phenoxy radical are 3.59, 2.48, and 2.29 eV respectively.

Channel 4 corresponds to the dissociation of the methyl phenoxy radical to two propargyl radicals and a formyl radical. The translational energy distribution for this channel is shown in Fig. 3.3.11 with maximum translational energies of 1.06, -0.05, and -0.23 eV for the meta, ortho, and para isomers respectively. The negative maximum dissociation energies for the ortho and para isomers suggest that there is not enough energy available at 6.42 eV to dissociate these isomers, so channel 4 is expected to be comprised entirely of the meta isomer at this energy. The maximum translational energy of 1.06 eV is marked on Fig. 3.3.11 with a red arrow. The maximum translational energy of this channel occurs very near the peak of the distribution, which is typically associated with excited state dissociation processes. However, the majority of

the fragments in the distribution have energies above the 1.06 eV maximum. Also, the dissociation of benzene to form two propargyl radicals has been studied previously and is believed to involve significant isomerization to take place.[33] For these reasons, it is much more likely that benzene dissociation occurs on the ground state as opposed to the excited state. The reason for the fragments in Fig 3.3.11 exceeding the maximum available energy is not known at this time. However, it may be caused by initial internal excitation from the detachment laser and/or multiple photon absorption.

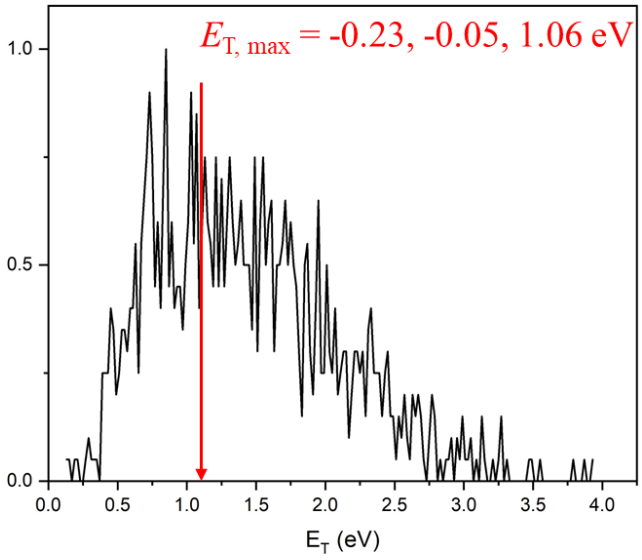


**Figure 3.3.11.** The translational energy distribution of dissociation channel 3 of the methyl phenoxy radical at 6.42 eV. The maximum translational energies for the meta, ortho, and para isomers of the methyl phenoxy radical are 1.06, -0.05, and -0.23 eV respectively. A red arrow is added to the plot to mark the maximum translational energy of the meta isomer at 1.06 eV.

# 3.4 Conclusions

The photodissociation dynamics of the methyl phenoxy radical are investigated using fast beam photofragment spectroscopy. A photoelectron spectrum was taken and confirmed the presence of the meta, ortho, and para methyl phenoxy radical isomers in the molecular beam. The isomers were not isolated and photodissociation is conducted on a mixture of all three isomers. Photodissociation was conducted at photon energies of 6.42 eV and revealed 4 dissociation channels.

Channel 1 is a 2-body dissociation channel resulting in fragments of benzene and a formyl radical. Channel 2 is a 3-body dissociation mechanism that results in dissociation fragments of benzene, carbon monoxide, and a hydrogen atom. Channel 2 likely follows channel 1 as a sequential dissociation mechanism as evidenced by the similar products which only differ by the further dissociation of the formyl radical for channel 1. Channel 3 is another 3-body dissociation channel that results in dissociation fragments of 1-buten-3-yne, carbon monoxide, and a vinyl radical. Channel 4 is a 3-body dissociation channel that results in a formyl radical and two propargyl radicals. Channel 4 appears to be another sequential dissociation mechanism continuing from channel 1, by further dissociating benzene to form 2 propargyl radicals. The branching ratios for the four channels are 83, 4, 7, and 5 % for channels 1, 2, 3, and 4 respectively.

The translational energy distributions for the first three channels peak far below the maximum allowed translational energy mechanisms suggesting that all three dissociation mechanisms are ground state processes. Dissociation for the first three channels likely proceeds via internal conversion to the ground state followed by statistical dissociation. The translational energy distribution for channel 4 peaks near the maximum translational energy of the meta isomer. This would normally be indicative of excited state dissociation, however, previous work on benzene dissociation and the majority of channel 4 fragments peaking above the maximum translational energy suggest that channel 4 is most likely a ground state dissociation process where additional energy has been imparted to the fragments from an unknown source.

# 3.5 References

[1] M. E. Tuckerman, and G. J. Martyna, J. Phys. Chem. B **104** (2000) 159.
[2] D. Herschbach, Faraday Discussions of the Chemical Society **55** (1973) 233.
[3] D. R. Herschbach, Discussions of the Faraday Society **33** (1962) 149.
[4] Y.-T. Lee *et al.*, Review of Scientific Instruments **40** (1969) 1402.
[5] A. Rahman, Phys. Rev. **136** (1964) A405.
[6] T. G. Shepherd, Chem. Rev. **103** (2003) 4509.
[7] J. W. Morse, and D. Rickard, Environmental science & technology **38** (2004) 131A.
[8] J. N. Eisenberg, D. H. Bennett, and T. E. McKone, Environmental science & technology **32** (1998) 115.
[9] C. L. Brooks III *et al.*, PNAS **95** (1998) 11037.
[10] J. Ingham *et al.*, *Chemical engineering dynamics: an introduction to modelling and computer simulation* (John Wiley & Sons, 2008), Vol. 3,
[11] S. Y. van de Meerakker *et al.*, Chem. Rev. **112** (2012) 4828.
[12] J. Jankunas, and A. Osterwalder, Annu. Rev. Phys. Chem. **66** (2015) 241.
[13] M. L. Weichman, and D. M. Neumark, Annu. Rev. Phys. Chem. **69** (2018) 101.
[14] D. L. Osborn *et al.*, J. Chem. Phys. **106** (1997) 3049.
[15] E. N. Sullivan, B. Nichols, and D. M. Neumark, Phys. Chem. Chem. Phys. **21** (2019) 14270.
[16] A. Kunin, and D. M. Neumark, Phys. Chem. Chem. Phys. **21** (2019) 7239.

[17] A. F. T. S. a. D. Registry, edited by E. P. Agency2008).
[18] Y. Abdollahi *et al.*, International Journal of Molecular Sciences **13** (2012) 302.
[19] C.-Y. Lin, and M.-C. Lin, J. Phys. Chem. **90** (1986) 425.
[20] A. Colussi, F. Zabel, and S. Benson, Int. J. Chem. Kinet. **9** (1977) 161.
[21] R. Buth, K. Hoyermann, and J. Seeba, in *Symp. (Int.) Combust.* (Elsevier, 1994), pp. 841.
[22] A. N. Morozov *et al.*, J. Phys. Chem. A **125** (2021) 3965.
[23] C. Fernholz, A. Bodi, and P. Hemberger, J. Phys. Chem. A **126** (2022) 9022.
[24] A. W. Harrison, (University of California – Berkeley, 2014).
[25] T. V. Sokolova *et al.*, Journal of Applied Spectroscopy **73** (2006) 632.
[26] L. S. Richard *et al.*, J. Phys. Chem. A **111** (2007) 8741.
[27] D. J. Nelson *et al.*, J. Chem. Phys. **146** (2017)
[28] W. Tsang, in *Energetics of organic free radicals* (Springer, 1996), pp. 22.
[29] M. W. Chase, J. Phys. Chem. Ref. Data **25** (1996) 551.
[30] M. J. Frisch *et al.*, Wallingford, CT, 2016).
[31] A. I. K. S. Gozem, P. Wojcik, S. Gozem, V. Mozhayskiy, in *The ezSpectra suite: An easy-to-use toolkit for spectroscopy modeling* ( WIRES CMS, 2021).
[32] J. M. Riveros, S. Ingemann, and N. M. Nibbering, J. Am. Chem. Soc. **113** (1991) 1053.
[33] V. V. Kislov *et al.*, J. Chem. Phys. **120** (2004) 7008.

# Chapter 4: Photodissociation of the Isoprene Hydroxy Radical at 248 nm

# 4.1 Introduction

Molecular dynamics is a field interested in the study of the microscopic movements and energy partitioning of molecules.[1] Both experimental and theoretical techniques to probe the dynamics of molecules and chemical reactions have been developed since the early 1960's.[2-5] These techniques have led to unprecedented levels of detail in the fundamental understanding of both reactive and non-reactive molecular motion which has played a significant role in countless fields including atmospheric chemistry, environmental science, biochemistry, and chemical engineering.[1, 6-10]

The development of molecular beam experiments in particular has been important to the understanding of molecular dynamics in a wide variety of fields.[11, 12] For more than thirty years, our research group has made use of various molecular beam experiments to study the molecular dynamics of many systems relevant in physics, chemistry, and biology.[13-16] The work performed in this chapter attempts to investigate the photodissociation dynamics of the isoprene hydroxy radical.

The isoprene hydroxy radical is a free radical species related to isoprene, the third most abundant hydrocarbon in the atmosphere.[17, 18] Isoprene is primarily released into the atmosphere by trees and vegetation, but is also released by humans, animals, and even bacteria.[19-22] Once in the atmosphere, isoprene reacts with hydroxy radicals to form several different species including the isoprene hydroxy radical and the much more stable isoprene hydroxy hydroperoxide (ISOPOOH).[17] Structures of isoprene, ISOPOOH, and the isoprene hydroxy radical are shown in Fig 4.1.1.

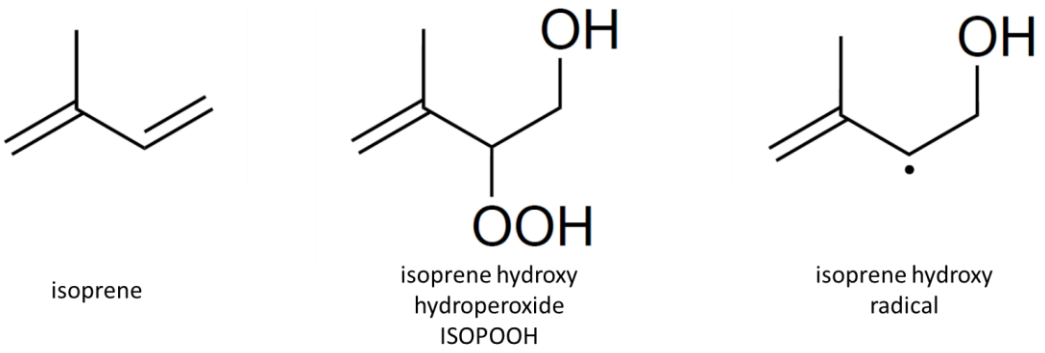


**Figure 4.1.1.** The structures of isoprene and its related compounds ISOPOOH and the isoprene hydroxy radical. Isoprene is the third largest source of hydrocarbons in the atmosphere.

The atmospheric abundance of isoprene and its products, makes these compounds of particular interest in developing a better understanding of their dynamics. While much work has been done on isoprene and ISOPOOH, little is known about the isoprene hydroxy radical.[17, 23-28] The isoprene hydroxy radical has been observed in several studies involving ISOPOOH and isoprene reactions, but to the best of our knowledge has not been investigated directly.[17, 27]

In this work our group proposes to investigate the photodissociation dynamics of the isoprene hydroxy radical using fast beam photodissociation spectroscopy. The relevant two and three-body dissociation channels are shown in Fig 4.1.2. Dissociation energies of each channel are calculated from the heats of formation of each species. Heats of formation for the product species are all taken from Tsang or Chase.[29, 30] The heat of formation for the isoprene hydroxy radical was calculated to be 3.73 eV. This calculated value was obtained from density functional theory with the B3LYP functional and 6 31G basis set using the ab initio quantum chemistry software Gaussian.[31]

| | | |
|---|---|---|
| Channel 1: | $C_5H_8OH \rightarrow OH + C_5H_8$ | $D_0 = 0.23$ eV |
| Channel 2: | $C_5H_8OH \rightarrow O + C_5H_9$ | $D_0 = 1.26\ eV$ |
| Channel 3: | $C_5H_8OH \rightarrow C_4H_5 + CH_3OH$ | $D_0 = -3.42\ eV$ |
| Channel 4: | $C_5H_8OH \rightarrow OH + CH_3 + C_4H_5$ | $D_0 = 0.62\ eV$ |
| Channel 5: | $C_5H_8OH \rightarrow O + CH_4 + C_4H_5$ | $D_0 = 0.51\ eV$ |

**Figure 4.1.2.** The relevant two and three-body dissociation channels of the isoprene hydroxy radical at 248 nm. All dissociation energies are calculated from heats of formation of the individual species. Heats of formation of the product species are taken from Tsang or Chase.[29, 30] The heat of formation for the isoprene hydroxy radical was calculated to be 3.73 eV using density functional theory with a B3LYP functional and 6 31G basis set from the quantum chemical software Gaussian.[31]

# 4.2 Experimental Methods

The photodissociation dynamics of the isoprene hydroxy radical are investigated using fast beam photofragment spectroscopy. The instrument used to perform these experiments is the fast radical beam machine (FRBM) described in detail in Chapter 2 Section 2 of this dissertation. The precursor molecule chosen for this experiment is ISOPOOH, the structure of which is shown in Fig. 4.1.1. ISOPOOH was chosen as a precursor since it is relatively stable in the liquid phase at room temperature and is likely to ionize by removal of part or all of its peroxide group in our electric discharge.[32-35]

ISOPOOH is not commercially available and was synthesized for the purpose of our experiment. Recently, more modern synthesis techniques for ISOPOOH have been documented.[33] However, at the time these experiments were conducted the synthesis outlined in the thesis of Lozano was followed.[32] This procedure was modified slightly for our purposes due to lack of the appropriate equipment; modifications from the original procedure are discussed in section A1 of the appendix. After completion of the first synthesis, characterization was done using proton NMR by a former graduate student Isaac Ramphal. The original NMR spectra has been lost; however, characterization is always performed through photoelectron spectroscopy in our instrument when a new batch of ISOPOOH is synthesized. Batches of ISOPOOH last about 2 weeks at room temperature before there is noticeable degradation of anion signal. For the purposes of the experiments described in this work 3 total batches of ISOPOOH were synthesized.

After synthesis, ISOPOOH is placed in a bubbler and ~30 psi of argon backing gas is bubbled through the sample and sent to the Amsterdam piezo valve. The ISOPOOH and backing gas are supersonically expanded into the source chamber through the electric discharge which creates the isoprene hydroxy anion shown in Fig 4.2.1. The electric discharge is comprised of two metal grids spaced 1 mm apart and held at a potential difference of ~2 kV.

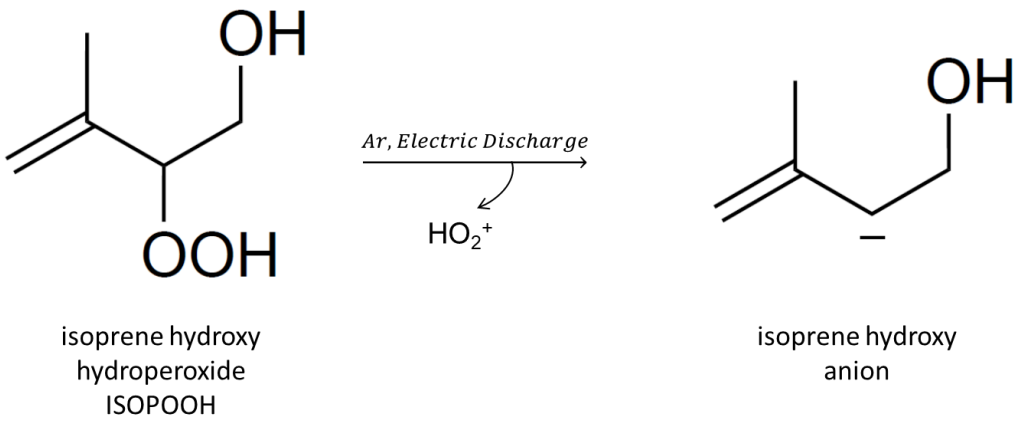


**Figure 4.2.1.** The reaction forming the isoprene hydroxy anion from ISOPOOH which takes place in the electric discharge of the FRBM. The electric discharge consists of two metal grids spaced 1 mm apart and held at a potential difference of ~2 kV.

The newly created isoprene hydroxy anions are mass filtered and sent to the first interaction region where they are photodetached at 532 nm (2.33eV) by a Nd-YAG (Litron) to form the isoprene hydroxy radical. This process is shown in Fig. 4.2.2. The detached electrons are detected by a velocity map imaging spectrometer (VMI) and a photoelectron spectrum is used to characterize the isoprene hydroxy radical. After characterization, the detachment laser

energy is then used to pump a dye laser (Radiant dyes) that is tuned to just above the electron affinity of the isoprene hydroxy radical at 501 nm (2.47 eV), and the radicals are sent to the second interaction region. In the second interaction region, the radicals are subjected to a 248 nm (5.00 eV) excimer laser (GAM) pulse and photodissociation is initiated. The photodissociation fragments are detected by a hexanode delay line detector which records the 2-dimentional position of the particles as well as their arrival times.

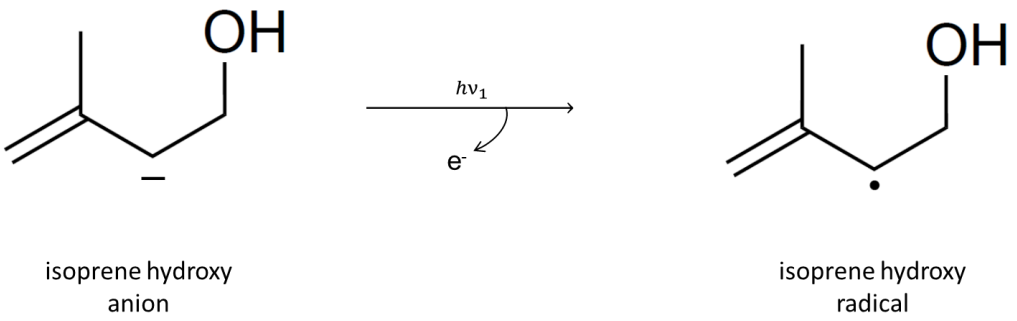


**Figure 4.4.2.** The formation of the isoprene hydroxy radical by photodetachment of the isoprene hydroxy anion. A 532nm (2.33 eV) or 501 nm (2.47 eV) photon detaches an electron from the isoprene hydroxy anion to form the isoprene hydroxy radical.

# 4.3 Results and Discussion

## 4.3.1 Photoelectron Spectrum

The photoelectron spectrum for the isoprene hydroxy radical is shown in Fig. 4.3.1. The photoelectron spectrum for the isoprene hydroxy radical is much noisier than most spectra that are taken using this spectrometer. The source of the noise is not known, but may be due to a slight misalignment of the detachment laser causing electrons to detach from the aluminum baffle in the first interaction region. The region of the photoelectron spectrum from 0.0 to 0.2 eV of electron kinetic energy is particularly noisy producing a broad peak that is nearly the size of the electron affinity peak at 0.20 eV (electron kinetic energy). Trying to obtain a clean photoelectron spectrum for this system proved to be difficult, and eventually it was decided to ignore the noisy parts of the spectrum.

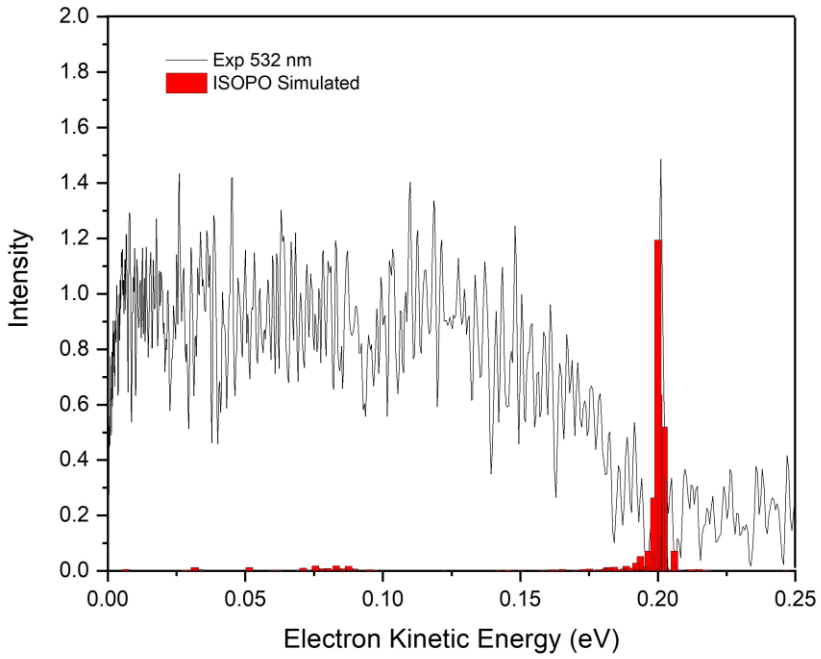


**Figure 4.3.1.** The photoelectron spectrum of the isoprene hydroxy anion at 532 nm (2.33 eV). The spectrum is quite noisy at low electron kinetic energies but shows a strong electron affinity peak at 0.20 eV (electron kinetic energy) corresponding to an electron binding energy of 2.46 eV.

The minimum energy points of the isoprene hydroxy anion and radical are calculated using the ab inito quantum chemistry software Gaussian, and the spectrum was simulated using eZFCF and is shown in red on Fig. 4.3.1.[31, 36] The electron affinity peak of the simulation was assigned and overlapped with the peak from the experimental spectrum. The simulated spectrum predicts only one large progression centered around the electron affinity, with very small peaks at lower electron kinetic energies which are masked by noise in the experimental spectrum. Apart from the noisy region, the simulated spectrum is in good agreement with the experimental spectrum, and it is likely that the species we are forming is the isoprene hydroxy radical.

The electron affinity of the isoprene hydroxy radical appears in the spectrum at electron kinetic energy of 0.20 eV which equates to a binding energy of 2.13 eV. The Nd-YAG detachment laser was then used to pump a dye laser tuned to 583nm (2.13 eV), just above the electron affinity of the radical. This process ensures that the radicals we are studying are in their ground vibrational state.

## 4.3.2 2-Body Mass Distribution

The isoprene hydroxy radicals entering the second interaction region are subjected to a 248 nm (5.00 eV) excimer laser pulse. Radicals that absorb a photon dissociate and the fragments are detected in coincidence on a hexanode delay line detector. The 2-body mass distribution for the dissociation of the isoprene hydroxy radical at 248 nm is shown in figure 4.3.2.

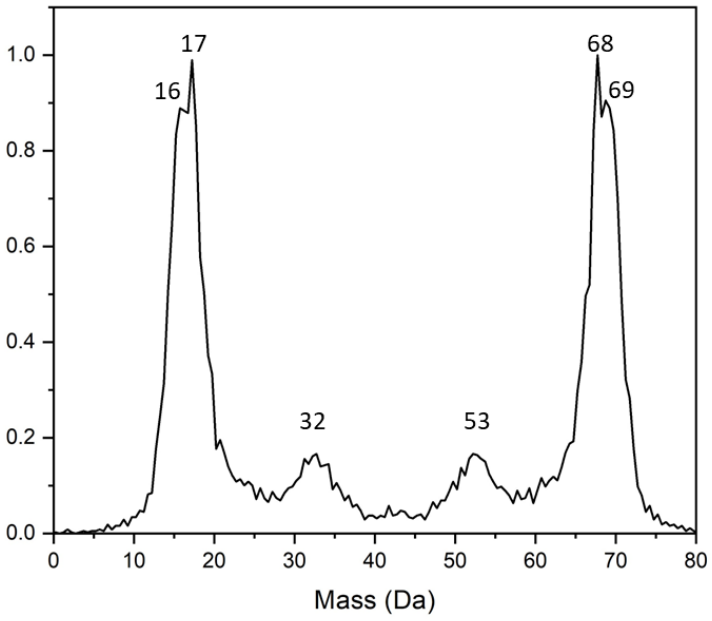


**Figure 4.3.2.** The 2-body mass distribution for the dissociation of the isoprene hydroxy radical at 248 nm (5.00 eV). The distribution shows peaks at 16, 17, 32, 53, 68, and 69 amu.

The 2-body mass distribution shows coincident pair peaks at 16 and 69 amu, 17 and 68 amu, as well as 32 and 53 amu. The simplest assignment to make is the peak pair at 17 and 68 amu. This pair is labeled channel 1 and is assigned to a hydroxy radical and isoprene. A depiction of channel 1 is shown in Fig. 4.3.3. Channel 1 is particularly easy to assign because the peak at 17 amu can only be a hydroxide radical, and the mechanism for this channel could easily be performed through a simple bond cleavage to remove the hydroxide radical and form a diradical on the hydrocarbon, then followed by forming a double bond to make isoprene.

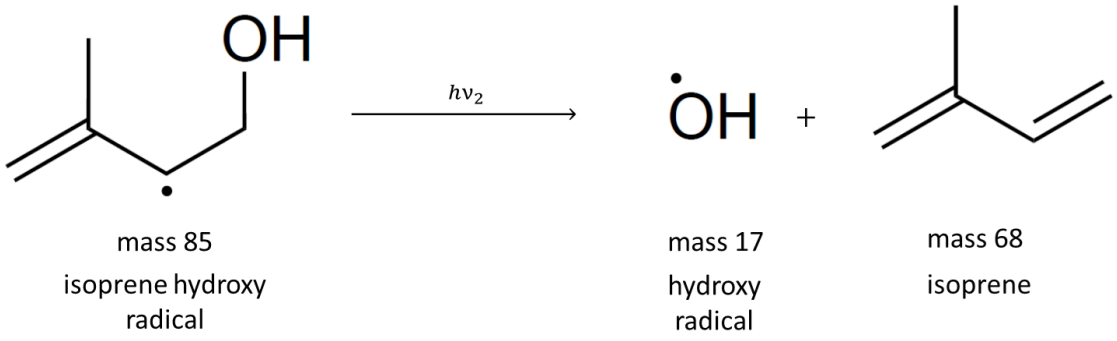


**Figure 4.3.3.** Channel 1 of the dissociation of the isoprene hydroxy radical at 248 nm. Channel 1 results in dissociation fragments of isoprene and a hydroxy radical.

The peaks in the 2-body distribution at 16 and 69 amu also only have one valid assignment. They are labeled as channel 2 and assigned to be an oxygen atom and 3-methyl-1-buten-3-yl. The dissociation of the isoprene hydroxy radical through channel 2 is shown in Fig. 4.3.4. Unlike channel 1 whose assignment is restricted by the low mass peak, channel 2 is restricted by the high mass peak. While mass 16 can be either oxygen or methane, to the best of our knowledge, no information on species with the chemical formula $C_4H_5O$ is available, meaning that the peak at 16 amu must be oxygen.[37]

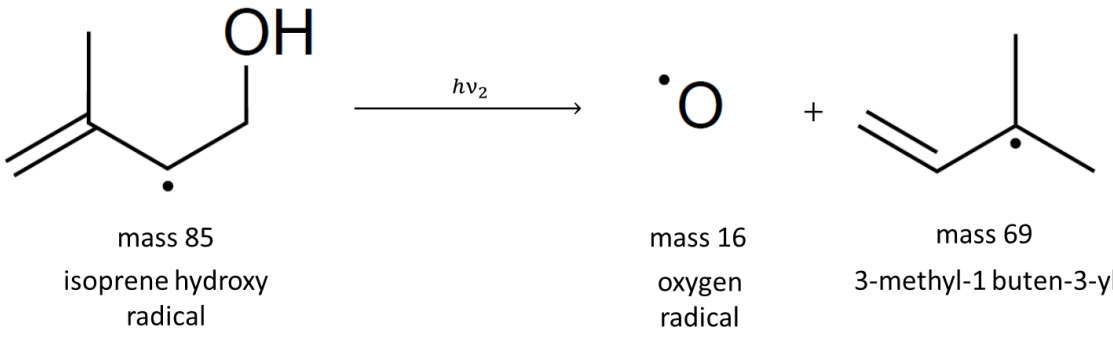


**Figure 4.3.4.** Channel 2 of the dissociation of the isoprene hydroxy radical at 248 nm. Channel 2 results in dissociation fragments of an oxygen radical and 3-methyl-1-buten-3-yl.

The coincidence pairs to be assigned in the 2-body distribution are the peaks at mass 32 and 53 amu. This channel is once again easy to assign as the only possible assignments for mass 32 are methanol ($CH_3OH$) and $C_2H_8$ only the first of which is known to exist.[37] The peaks at mass 32 and 53 amu are labeled channel 3 and assigned to methanol and 1-butyn-3-yl which is chosen because it is the lowest energy structure known to exist at mass 53. The 2-body dissociation channel 3 of the isoprene hydroxy radical is shown in figure 4.3.5.

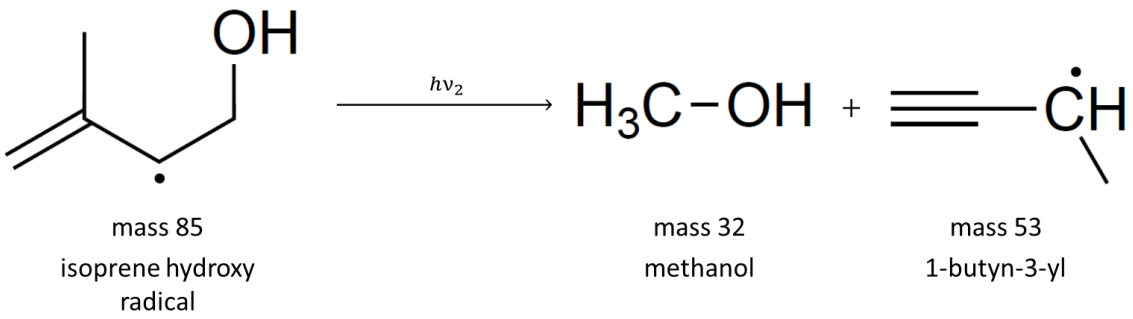


**Figure 6.4.5.** Channel 3 of the dissociation of the isoprene hydroxy radical at 248 nm. Channel 3 results in dissociation fragments of methanol and 1-butyn-3-yl.

## 4.3.3 3-Body Mass Distribution

The three body mass distribution of the isoprene hydroxy radical is shown in Fig. 4.3.6, and only displays two broad peaks at 16 and 53 amu. The peak at 16 amu is approximately double the intensity of the peak at 53 amu suggesting that two similar mass fragments are overlapping and creating a combined peak at 16 amu. Based on this fact, the most obvious assignment for the 3-body dissociation channel appearing in this distribution is to assign the peak centered at 16 amu to be a combination of hydroxide radical of mass 17 amu and a methyl radical at mass 15 amu, this would result in 1-butyn-3-yl as the third species at mass 53. This assignment is labeled channel 4 and displayed in Fig. 4.3.7. However, while the peak at 53 amu is very likely 1-butyn-3-yl, the other two fragments could also be oxygen and methane which is a much lower energy combination of products labeled channel 5 and displayed in Fig. 4.3.8.

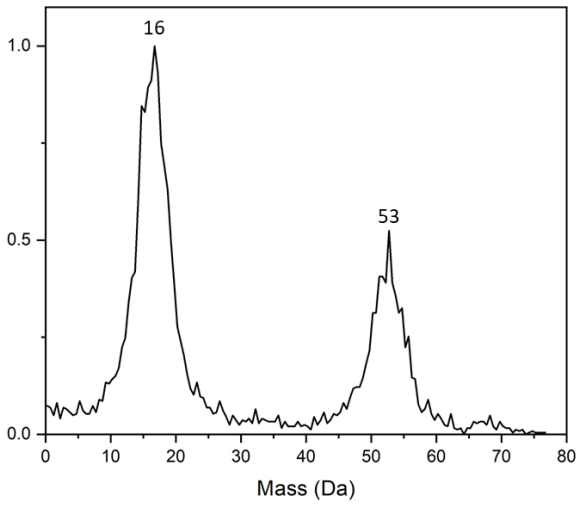


**Figure 4.3.6.** The 3-body mass distribution of the dissociation of the isoprene hydroxy radical at 248 nm. The distribution shows two peaks, a peak at mass 53 and a peak at mass 16 that is approximately double the intensity.

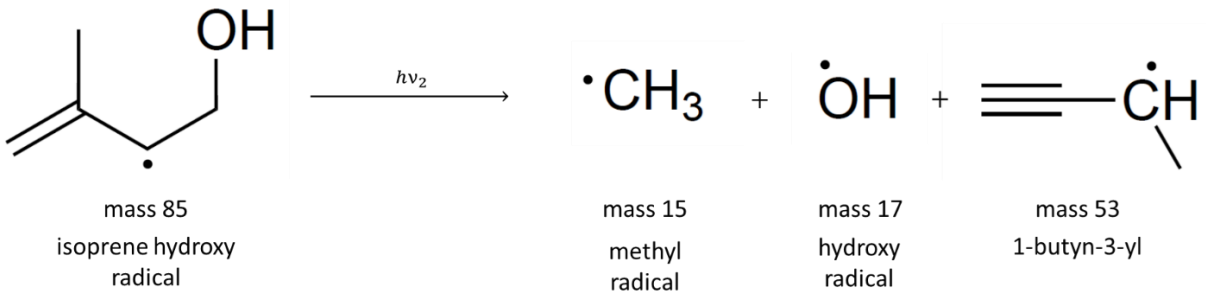


**Figure 4.3.7.** Channel 4 of the dissociation of the isoprene hydroxy radical at 248 nm. Channel 4 results in dissociation fragments of a methyl radical, hydroxy radical, and 1-butyn-3-yl.

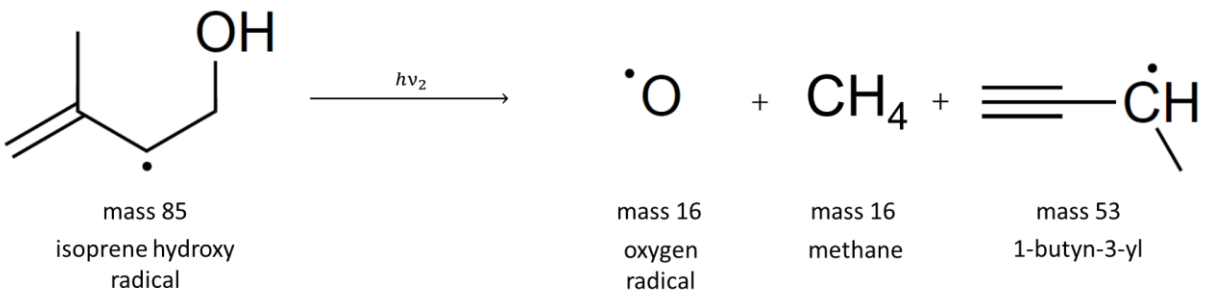


**Figure 4.3.8.** Channel 5 of the dissociation of the isoprene hydroxy radical at 248 nm. Channel 5 results in dissociation fragments of oxygen, methane, and 1-butyn-3-yl.

It is unclear whether the 3-body dissociation of isoprene hydroxy corresponds to channel 4, channel 5, or both. While channel 5 is significantly lower energy than channel 4 with dissociation energies of 0.51 and 0.62 eV respectively, channel 4 can easily proceed as a sequential mechanism from channel 3. Channel 4 may proceed by dissociating to form methanol and 1-butyn-3-yl via channel 3, and then further dissociating the methanol fragment to hydroxide and a methyl radical. This sequential dissociation process would happen through a simple bond cleavage; however, it would require 4.04 eV being partitioned into the methanol fragment to happen.[30] The available energy for this channel is 8.42 eV owing to the highly stable methanol product, so this mechanism is highly probable. Despite channel 5 being lower energy, and therefore a more likely candidate for the 3-body dissociation channel, channel 4 cannot be ruled out and further experiments would need to be conducted to separate these two channels.

## 4.3.4 Branching Ratios

Two body dissociation events which include channels 1, 2, and 3 account for 86 % of the total dissociation events for the isoprene hydroxy radical at 248 nm. Channel 4 or 5, which is the only 3-body channel, accounts for the remaining 14 % of dissociation. Of the 2-body channels, channel 1 accounts for 41 % of the total dissociation, channel 2 accounts for 37 %, and channel 3 accounts for 7 %.

Given that channel 3 is the most stable product channel with the smallest dissociation energy, it's unexpected that this channel would result in the smallest branching ratio. Channel 4 which is possibly a sequential dissociation channel continuing from channel 3 makes up 14 % of the total dissociation events, so if they are sequential events, they would account for a total of 21 % of all dissociation. Channel 4 having a higher branching ratio than channel 3 is strong evidence that channel 4 is a sequential dissociation channel; however, 21 % is still much less than the branching ratios of the other two channels, and channel 4 might actually be events from

channel 5 or a mixture of the two as discussed earlier. Channel 2 in particular has the highest dissociation energy and has a branching ratio 16 % higher than the combined channel 3 and 4. Although no explanation for this phenomenon is offered in this work, any possible explanation must lie in the mechanism for channel 3. It is reasonable that a relatively high activation energy barrier must be reached to form the transition state for this channel, but further work would need to be performed to say for certain.

### 4.3.5 Translational Energy Distributions

The hexanode delay line detector collects arrival times and positions of the dissociation fragments that are used along with the masses assigned to construct translational energy distributions for each product channel. The translational energy distribution for channel 1 is displayed in Fig. 4.3.9 and the maximum translational energy $E_{\mathrm{T,max}}$ is listed in red at the top of the chart. The dissociation energy for channel 1 is 0.23 eV corresponding to a maximum translational energy of 4.77 eV at dissociation photon energy of 5.00 eV (248 nm).[29, 30] The channel 1 translational energy distribution peaks around 0.4 eV which is far less than the maximum translational energy and is indicative of a ground state dissociation process. In a ground state dissociation process, the excited radical must undergo internal conversion to the ground state before statistical dissociation will occur. In ground state dissociation, the vast majority of the energy imparted by the photon is partitioned to internal degrees of freedom and not translation so $E_{\mathrm{T}} \ll E_{\mathrm{T,max}}$.

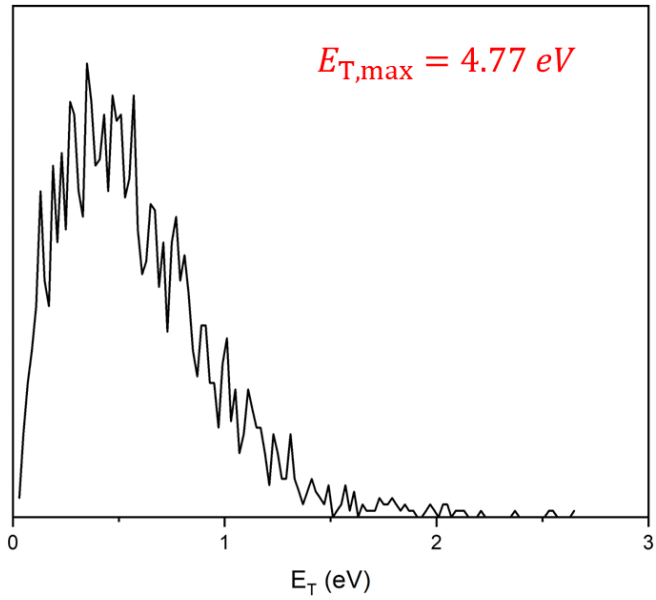


**Figure 4.3.9.** The translational energy distribution for channel 1 of the dissociation for the isoprene hydroxy radical at 5.00 eV. The distribution peaks around 0.4 eV and the maximum translational energy is 4.77 eV.

Channel 2 of the isoprene hydroxy radical dissociation has the highest dissociation energy of all four channels at 1.26 eV.[29, 30] This dissociation energy corresponds to a maximum translational energy of 3.74 eV. The translational energy distribution for channel 2 is shown in Fig 4.3.10 and peaks around 0.2 eV meaning that the translational energy of the fragments is once again far less than the maximum available translational energy. This trend is once again indicative of ground state dissociation and channel 2 likely proceeds via internal conversion to the ground state followed by statistical dissociation.

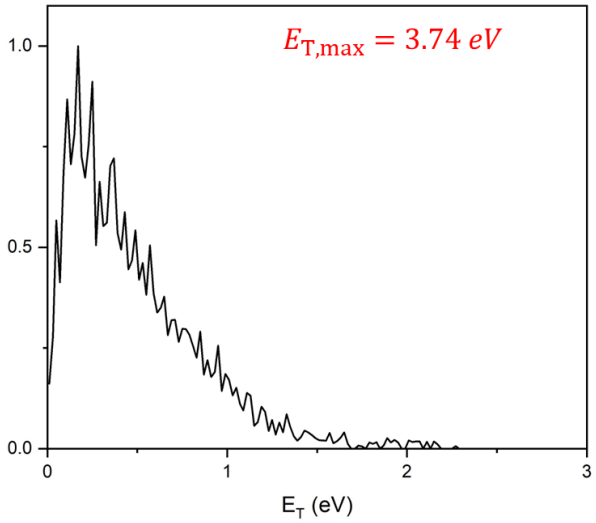


**Figure 4.3.10.** The translational energy distribution for channel 2 of the dissociation for the isoprene hydroxy radical at 5.00 eV. The distribution peaks around 0.2 eV and the maximum translational energy is 3.74 eV.

The translational energy distribution of channel 3 for the dissociation of the isoprene hydroxy radical is shown in Fig. 4.3.11 and has a dissociation energy of -3.42 eV.[29, 30] The negative dissociation energy suggests that the products of channel 3 are much more stable than the isoprene hydroxy radical itself. The stability of the products is credited to the methanol fragment which has a enthalpy of formation of -205 kJ/mol.[30] The corresponding max translational energy for channel 3 at a 5.00 eV photon energy is 8.42 eV. The translational energy distribution of channel 3 peaks around 0.25 eV which is far less than the maximum, suggesting that channel 3 is also a ground state dissociation process.

The relatively small dissociation energy of channel 3 yields 8.42 eV of energy available for the products. For channel 4 to follow channel 3 as a sequential dissociation event, 4.04 eV of energy must be partitioned into the methanol fragment during dissociation, which is less than half of the available energy. This would mean that we expect to see a fairly large percentage of channel 3 dissociation events continue to channel 4, which is likely what we observe as the branching ratios are 7 % and 14 % for channels 3 and 4 respectively. If future experiments were possible, lowering the dissociation photon energy would help confirm this hypothesis.

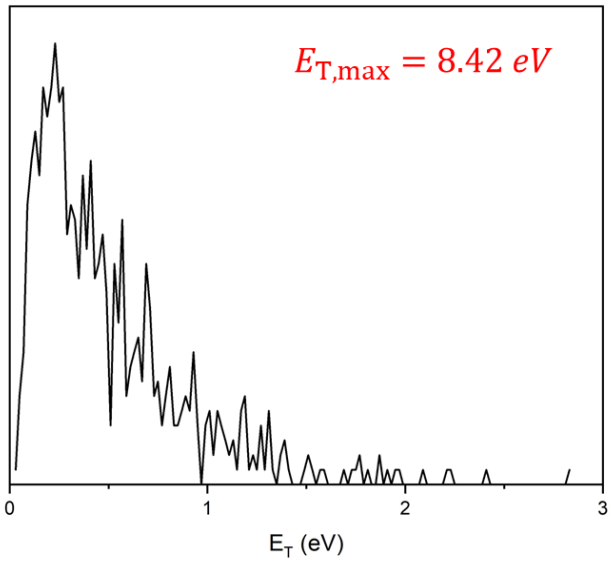


**Figure 4.3.11.** The translational energy distribution for channel 3 of the dissociation for the isoprene hydroxy radical at 5.00 eV. The distribution peaks around 0.3 eV and the maximum translational energy is 8.42 eV.

Channel 4 or 5 is the only 3-body dissociation channel for the isoprene hydroxy radical. Channel 4 has a dissociation energy of 0.62 eV and channel 5 has a dissociation energy of 0.51 eV which correspond to maximum translational energies of 4.38, and 4.49 eV at a photon energy of 5.00 eV. The translational energy distribution for channel 4 is shown in Fig. 4.3.12 and peaks around 0.7 eV which is far below the maximum kinetic energy for both channel 4 and 5, and once again indicative of ground state dissociation.

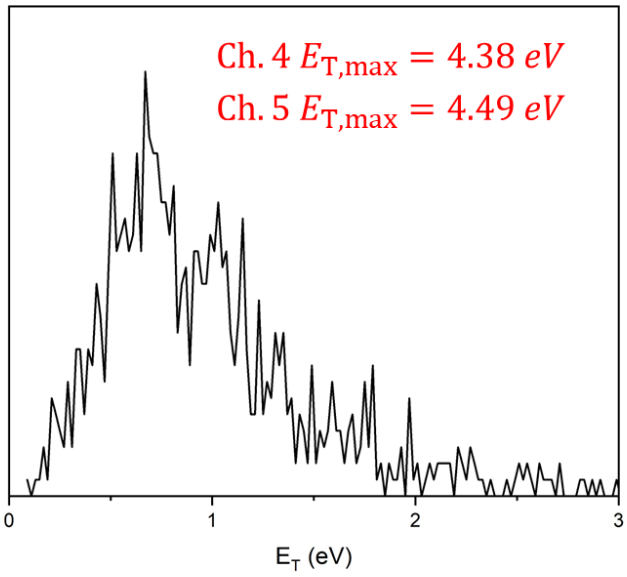


**Figure 4.3.12.** The translational energy distribution for channel 4 or channel 5 of the dissociation of the isoprene hydroxy radical at 5.00 eV. The distribution peaks around 0.7 eV and the maximum translational energy is 4.38 eV for channel 4 and 4.49 eV for channel 5.

# 4.4 Conclusions

The photodissociation dynamics of the isoprene hydroxy radical are investigated using fast beam photofragment spectroscopy. A photoelectron spectrum of the isoprene hydroxy anion was taken at 532 nm and the presence of the isoprene hydroxy radicals in the molecular beam is suspected. This along with proper mass selection are evidence to continue with photodissociation of the radical. The wavelength of the detachment laser was adjusted to 538 nm, just above the energy of the electron affinity peak found in the photoelectron spectrum before starting dissociation experiments.

Photodissociation was carried out at 248 nm (5.00 eV) and 4 dissociation channels were found. Channel 1 is a 2-body channel that consists of a hydroxide radical and isoprene, it makes up 41 % of total dissociation events. Channel 2 is a 2-body channel that consists of an oxygen radical and 3-methyl-1-buten-3-yl which makes up 37 % of total dissociation. Channel 3 is the last 2-body channel and consists of methanol and 1-buten-3-yl. Despite being the most stable product channel, channel 3 only represents 7 % of the total dissociation events. Channel 4 or 5 make up the only 3-body channel consisting of a hydroxide radical, a methyl radical, and 1-buten-3-yl for channel 4, and oxygen, methane, and 1-buten-3-yl for channel 5. Channel 4 or 5

make up the remaining 14 % of the total dissociation events. The 3-body dissociation for the isoprene hydroxy radical may be comprised of channel 4, channel 5, or a combination of both. Further experiments are needed to decouple these two channels.

Translational energy distributions are plotted for each dissociation channel. The translational energy for all five channels is far less than the maximum available energy that could go to translation. This is indicative of all 5 dissociation mechanisms proceeding via internal conversion to the ground state followed by statistical dissociation.

The products of channel 4 suggest that channel 4 is most likely a sequential dissociation event that proceeds from channel 3. When dissociation occurs via channel 3, a partitioning of 4.04 eV or more of the available 8.42 eV into the methanol fragment may result in further dissociation of the methanol to form a hydroxide radical and methyl radical. The large quantity of available energy and 14 % branching ratio for channel 4 compared to only 7 % for channel 3 provide strong evidence to support the mechanism for channel 4 being a sequential dissociation continued from channel 3.

# 4.5 References

[1] M. E. Tuckerman, and G. J. Martyna, J. Phys. Chem. B **104** (2000) 159.
[2] D. Herschbach, Faraday Discussions of the Chemical Society **55** (1973) 233.
[3] D. R. Herschbach, Discussions of the Faraday Society **33** (1962) 149.
[4] Y.-T. Lee *et al.*, Review of Scientific Instruments **40** (1969) 1402.
[5] A. Rahman, Phys. Rev. **136** (1964) A405.
[6] T. G. Shepherd, Chem. Rev. **103** (2003) 4509.
[7] J. W. Morse, and D. Rickard, Environmental science & technology **38** (2004) 131A.
[8] J. N. Eisenberg, D. H. Bennett, and T. E. McKone, Environmental science & technology **32** (1998) 115.
[9] C. L. Brooks III *et al.*, PNAS **95** (1998) 11037.
[10] J. Ingham *et al.*, *Chemical engineering dynamics: an introduction to modelling and computer simulation* (John Wiley & Sons, 2008), Vol. 3,
[11] S. Y. van de Meerakker *et al.*, Chem. Rev. **112** (2012) 4828.
[12] J. Jankunas, and A. Osterwalder, Annu. Rev. Phys. Chem. **66** (2015) 241.
[13] M. L. Weichman, and D. M. Neumark, Annu. Rev. Phys. Chem. **69** (2018) 101.
[14] D. L. Osborn *et al.*, J. Chem. Phys. **106** (1997) 3049.
[15] E. N. Sullivan, B. Nichols, and D. M. Neumark, Phys. Chem. Chem. Phys. **21** (2019) 14270.
[16] A. Kunin, and D. M. Neumark, Phys. Chem. Chem. Phys. **21** (2019) 7239.
[17] J. M. St. Clair *et al.*, J. Phys. Chem. A **120** (2016) 1441.
[18] A. Guenther *et al.*, Atmos Chem Phys **6** (2006) 3181.
[19] T. D. Sharkey, A. E. Wiberley, and A. R. Donohue, Annals of Botany **101** (2007) 5.
[20] J. King *et al.*, Journal of Theoretical Biology **267** (2010) 626.
[21] A. Johnston *et al.*, Environmental Microbiology **19** (2017) 3526.

[22] D. Gelmont, R. A. Stein, and J. F. Mead, Biochemical and Biophysical Research Communications **99** (1981) 1456.
[23] M. A. Allodi, K. N. Kirschner, and G. C. Shields, J. Phys. Chem. A **112** (2008) 7064.
[24] P. Campuzano-Jost *et al.*, J. Phys. Chem. A **108** (2004) 1537.
[25] E. Dovrou *et al.*, Atmos Chem Phys **21** (2021) 8999.
[26] H. Fuchs *et al.*, Nature Geoscience **6** (2013) 1023.
[27] J. Rivera *et al.*, in *EGU General Assembly Conference Abstracts*2015), p. 5378.
[28] Y. Zhang *et al.*, in *2021 AAAR 39th Annual Conference*2021).
[29] W. Tsang, in *Energetics of organic free radicals* (Springer, 1996), pp. 22.
[30] M. W. Chase, J. Phys. Chem. Ref. Data **25** (1996) 551.
[31] M. J. Frisch *et al.*, Wallingford, CT, 2016).
[32] E. I. Lozano, in *California State University, Fresno*2015).
[33] P. Mettke *et al.*, Atmosphere **13** (2022) 507.
[34] B. Nichols *et al.*, J. Chem. Phys. **147** (2017)
[35] E. N. Sullivan, B. Nichols, and D. M. Neumark, J. Chem. Phys. **148** (2018)
[36] A. I. K. S. Gozem, P. Wojcik, S. Gozem, V. Mozhayskiy, in *The ezSpectra suite: An easy-to-use toolkit for spectroscopy modeling* ( WIRES CMS, 2021).
[37] N. I. o. S. a. Technology, 2023).

# Chapter 5: Flat Liquid Jet Scattering Experimental Methods

# 5.1 Experimental Scheme

Liquid jet scattering provides a method for probing dynamics at the gas-liquid interface. Two limiting mechanisms at the gas liquid interface that our experiment seeks to differentiate and characterize are impulsive scattering (IS) and thermal desorption (TD). Impulsive scattering occurs when gas molecules collide with the liquid surface and are quickly recoiled in a nearly elastic collision.[1, 2] Thermal desorption on the other hand refers to a process where the gas molecule is trapped by the liquid and desorbs at a later time statistically following a Maxwell-Boltzmann (MB) distribution. A schematic comparing IS and TD is shown in Fig. 5.1.1.

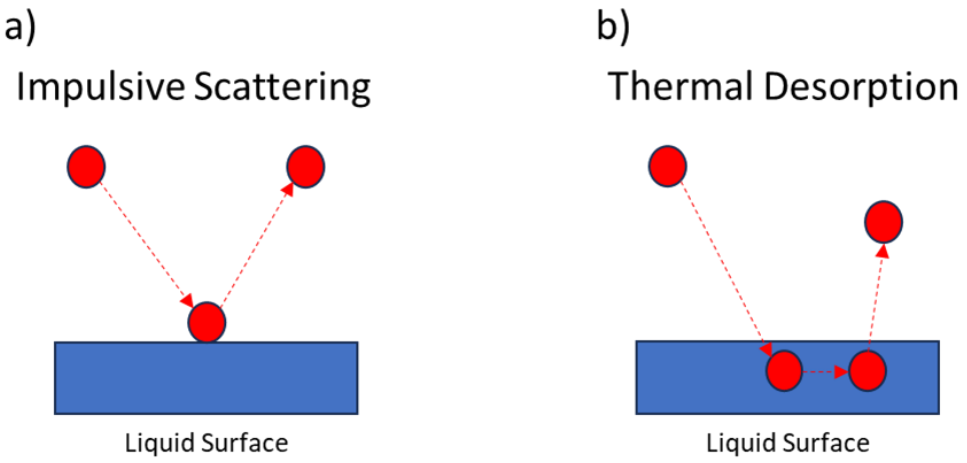


**Figure 5.1.1.** Schematic of a) impulsive scattering and b) thermal desorption mechanisms for gas-liquid scattering.

In gas liquid scattering experiments, TD is characterized by an MB distribution at the liquid temperature, because the trapped gas molecules have time to thermalize with the liquid before they are desorbed. IS on the other hand is characterized by the distribution of the impeding molecule. In the case of our experiment, our gas molecules are introduced into vacuum via a supersonic expansion and thus follow a supersonic (SS) distribution. By comparing and fitting the time of flights of scattered gas particles, it is possible to characterize their scattering mechanism and understand the dynamics of the scattering process.

# 5.2 Flat Liquid Jet Scattering

## 5.2.1 Instrument Schematic

The flat liquid jet scattering apparatus is shown in figure 5.2.1. The instrument schematic shown in figure 5.2.1 includes only the parts of the instrument that are unique to our experiment and excludes many of the experimental details. The remainder of this section will focus on a detailed dive into those unique parts of the instrument.

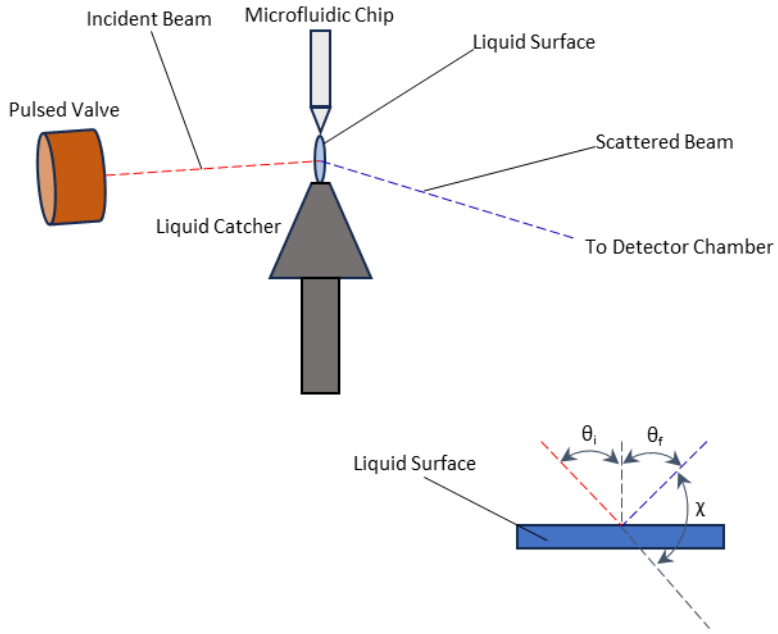


**Figure 5.2.1.** Schematic of the unique portions of the flat liquid jet scattering (FLJS) instrument.

## 5.2.2 Molecular Beam

The molecular beam for the experiment is generated using an Amsterdam piezoelectric valve (MassSpecpecD BV, Enschede). [3, 4] The opening time and voltage of the valve are varied depending on the optimization parameters of the system being studied, but generally fall around ~30 µs and ~160 V. In the case that the gas system being studied is a gas at room temperature, it is either studied directly or seeded in helium or argon in concentrations between 0.5 % and 10 %. In the case that the gas molecules being studied are a liquid at room temperature, the liquid is placed in a bubbler and a helium or argon backing gas is used. In all cases up to this point, the

backing pressure of the gas in the valve is 4 bar. The valve is jacketed and connected to a heater as well as a cooling reservoir for temperature controls ± 1 °C. After entering the chamber, the gas molecules undergo supersonic expansion and are skimmed twice with 500 µm skimmers before entering the main chamber.

## 5.2.3 Flat Liquid Jet

The flat liquid jet in our instrument is generated with the help of a commercially available microfluidic chip (Micronit). The chip has two 50 µm channels which generate two liquid jets and collide at the tip forming the series of liquid sheets used in the experiment. A schematic of this chip is shown in Fig 5.2.2.

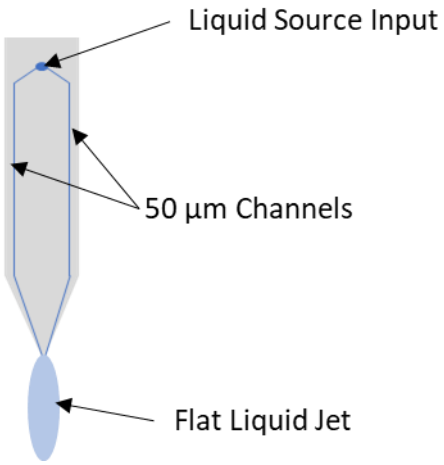


**Figure 5.2.2.** Schematic of the Micronit microfluidic chip. Pressurized liquid is introduced at the liquid source inlet, it continues down the two channels forming cylindrical jets that collide at the chip tip forming a flat liquid jet.

### 5.2.4 Liquid Source

The liquid provided to the Micronit chip can come from two different sources. Non-corrosive liquids such as dodecane are pumped into the chip from a high-performance liquid chromatography (HPLC) pump (Agilent). Liquids fed into the chip using the HPLC pump are held in an HPLC solvent bottle near the pump head and held close to ambient pressure with a constant stream of helium bubbled through the liquid to prevent atmospheric gases from interfering.

Corrosive liquids such as 8 M LiBr in water can damage the pump head and must be placed in a stainless-steel pressurized reservoir. The stainless-steel reservoir has a glass insert to prevent the liquid from corroding the metal, and a standard 1/8” tube equipped with a 200 μm particle filter. The reservoir is pressurized using any inert backing gas that will not interfere with the measurement up to 100 bar.

Once liquids leave the reservoir, they enter a double walled cooling system that is constantly being circulated by a temperature controlled 50:50 mixture of ethylene glycol and water. The double-walled cooling system is proficient at getting the liquid down to temperatures at or around -20 °C. Recently, work with salty water has elucidated the need for liquid temperatures below the capability of the cooling system, and several redesigns have been made that will not be discussed in this dissertation.

### 5.2.5 Liquid Catcher

Once the liquid in the jet has been pumped through the main chamber it is drained into the liquid catcher system. The liquid catcher system consists of a temperature-controlled copper skimmer placed vertically below the jet attached to a tigon tube that allows the liquid to drain into an HPLC solvent collection bottle which is cooled in an ice bath and evacuated by a mechanical pump. The principle behind this design is to heat the liquid copper skimmer to avoid liquid freezing and clogging the orifice, then rapidly cool the liquid when it enters the collection bottle to prevent back pressure from disturbing the jet.

### 5.2.6 Translational Stage and Cameras

One of the most difficult parts of running a liquid jet scattering experiment is getting everything properly aligned. Small deviation in the position of the jet relative to the liquid catcher can cause the entire experiment to be shut down for the day even if the misalignment only happenes for a fraction of a second. Also, misalignment with the molecular beam can prevent scattering from occurring as expected. For this reason, the microfluidic chip and catcher are placed on a translational and rotational stage to allow them to be moved relative to the other parts of the experiment. Aligning the jet is done manually using two cameras that are pointed at the experiment through viewing windows from two perpendicular directions. The cameras allow for the precise alignment of the jet and catcher relative to the each other and the molecular beam.

### 5.2.7 Detector

The particles are detected using a rotatable mass spectrometer that is well described in previous work.[1, 2] The detector consists of a quadrupole, ionizer, and ion detection assembly. The rotation of the detector combined with the rotational capabilities of the jet allow us to vary both the incident and detector angles of our scattered particles.

# 5.3 Data Analysis

The raw data obtained from scattering experiments are the time-of-flight profiles for the scattered species. The raw data is then fed into a data analysis program written in python by former graduate student Chin Lee and modified by current graduate student Walt Yang. The code for the python analysis program is contained in appendix section A2. The analysis program provides fitting for time-of-flight distributions, angular data through integration, and fitting to the soft-sphere and hard-sphere model.

Evaporation profiles are fit with a sum of two MB distributions. Scattering is fit with a sum of an MB distribution and SS distribution. TD fractions are obtained by dividing the integrated TD channel by the integrated IS channel in a scattering experiment.

# 5.4 References

[1] C. Lee *et al.*, J Phys Chem A **126** (2022) 3373.
[2] W. Yang *et al.*, J Chem Phys **159** (2023)
[3] D. Irimia *et al.*, Review of Scientific Instruments **80** (2009)
[4] C. Meng, and M. H. Janssen, Review of Scientific Instruments **86** (2015)

# Chapter 6: Molecular Beam Scattering of Ammonia from a Dodecane Flat Liquid Jet

# 6.1 Abstract

$ND_3$ evaporation and scattering from a dodecane flat liquid jet are investigated and compared to previous molecular beam scattering studies from liquid surfaces. Evaporation experiments are fitted and well-described by a Maxwell–Boltzmann flux distribution with a $\cos\theta$ angular distribution at the liquid temperature. Scattering experiments at $E_i = 28.8$ kJ mol$^{-1}$ and a deflection angle of 90° yield a thermal desorption fraction of 0.54 which is ~4 % higher than other molecules previously scattered from dodecane and consistent with work performed on $NH_3$ scattering from a squalane wetted wheel. $ND_3$ scattering from dodecane results in super-specular scattering that has been observed prior with other small molecular scattering from dodecane. The impulsive scattering channel is fitted to a "soft-sphere" model, yielding an effective surface mass of 55 amu and an internal excitation of 5.08 kJ mol$^{-1}$. Compared to our prior studies, impulsively scattered $ND_3$ behaves similar to other small molecules scattered from dodecane.

# 6.2 Introduction

The gas–liquid interface plays a key role in several processes including but not limited to acid rain formation, aerosol surface chemistry, and carbon capture at the ocean surface.[1-4] While significant work has been done previously to study the gas–liquid interface, elucidation of mechanistic detail behind gas–liquid interactions has remained a challenging endeavor.[5] Recent efforts by Nathanson and others, however, have allowed for the use of molecular beam scattering to study the gas–liquid interface[5-7]. This has given rise to uncovering mechanistic detail at a degree greater than what was previously possible for this critical chemical environment.

Molecular beam scattering is an incredibly powerful technique that has been used for over half a century to study chemical dynamics.[8-16] Advances in molecular beam scattering techniques have allowed for the elucidation of the dynamics and mechanistic details of several classes of chemical reactions. The major challenge of performing molecular beam scattering techniques on the gas–liquid interface is that the liquid must be compatible with a vacuum environment. The original molecular beam experiments performed to probe the gas–liquid interface were done with a wetted wheel which allowed for the study of liquids with vapor pressures below $10^{-3}$ Torr.[17-21]

More volatile liquids have been studied largely through the efforts of Faubel and co-workers who developed a liquid microjet which allows for these liquids to be vacuum compatible.[22, 23] While liquid microjets allow for the study of a larger array of liquids than the wetted wheel, they pose specific problems when attempting molecular beam scattering experiments. First, they provide poor signal-to-noise ratios due to the relatively small diameter of the jet. Second, the cylindrical nature of a typical microjet does not allow for angularly-resolved scattering measurements.[7] Taking these considerations into account, our group incorporated a flat

liquid jet into molecular beam scattering experiments using a microfluidic chip. The flat liquid jet is formed by colliding two cylindrical microjets to form a flat surface, which provides a much larger scattering target (~1 mm). This simultaneously solves the issues of low signal-to-noise ratios and loss of angular specificity.

The development of the flat liquid jet motivated two recent studies by our research group where Ne, $CD_4$, and $D_2O$ were scattered from dodecane.[24, 25] Dodecane was chosen as a target liquid specifically because of its relatively high vapor pressure ($1.5 \times 10^{-2}$ Torr at 275 K).[23] The choice of molecules to scatter from the dodecane jet followed from them all sharing a mass of 20 amu, but varying other physical properties, such as dipole moment, polarizability, and solubility.

Our studies compared two limiting scattering mechanisms, impulsive scattering (IS) and thermal desorption (TD).[24, 25] Impulsive scattering is characterized by an elastic or nearly elastic collision with the surface resulting in a scattered molecule that maintains much of the character of the incident molecular beam. Conversely, thermal desorption is characterized by a scattered particle being trapped at the liquid surface for a period of time long enough to thermalize with the liquid and then evaporate according to a Maxwell–Boltzmann flux distribution at the liquid temperature ($T_{liq}$).[5, 12, 26, 27]

In our previous work, we demonstrated that both the fractional energy loss and TD fraction, defined as TD/(TD + IS), are higher for the polyatomic molecules than they are for Ne, and trend in a consistent manner with the free energy of solvation found in literature.[25] These results also agreed with previous work performed by Nathanson scattering these same small molecules from squalane using a wetted wheel, although his study was confined to a single deflection angle.[28]

In this work, we aim to further investigate the scattering of small molecules from a dodecane flat liquid jet, by scattering deuterated ammonia ($ND_3$). $ND_3$ scattering naturally follows from our previous work[24, 25] as it has a mass of 20 amu and has previously been scattered from squalane by Nathanson.[28] This enables further comparison of trends between squalane and dodecane surfaces. $ND_3$ has very similar physical properties to $D_2O$ as shown in Table 6.1.1, apart from its polarizability which is nearly half that of $D_2O$.[28-30] Another interesting property of $ND_3$ is that it has the lowest energy vibrational mode of all of the molecules we have studied thus far: an umbrella inversion mode at 8.95 kJ $mol^{-1}$.[28, 31-34]

**Table 6.1.1.** Physical properties of $D_2O$ and $ND_3$.[25, 28-30, 35]

| **Physical Properties** | **$D_2O$** | **$ND_3$** |
|---|---|---|
| Radius (Å) | ~1.4 | ~1.8 |
| Polarizability ($Å^3$) | 2.2 | 1.3 |
| Dipole Moment (D) | 1.8 | 1.4 |
| Solubility in Hexadecane $K_H$ ($x_{soln}/P_{vap}$) | $2.17 \times 10^{-2}$ | $2.97 \times 10^{-2}$ |

# 6.3 Experimental Methods

The crossed molecular beam apparatus used for all experiments carried out in this work has been previously described in great detail.[24, 25, 36, 37] The instrument itself is comprised of three regions evacuated by turbomolecular pumps. The source region houses a piezoelectric pulsed valve (MassSpecpecD BV, Enschede) that generates the molecular beam.[38, 39] The collision chamber contains the flat liquid jet and is where gas–liquid interactions take place during scattering experiments. Also present within the collision chamber is a cryogenically cooled copper wall that assists in evacuating this region through cryo-condensation.[24, 25] Finally, the rotatable detector region is contained within the collision chamber and houses an electron impact ionizer, a quadrupole mass filter, and an ion detection assembly.[24, 25, 36, 37] Schematic diagrams of the scattering experimental configuration is shown in Fig. 6.3.1.

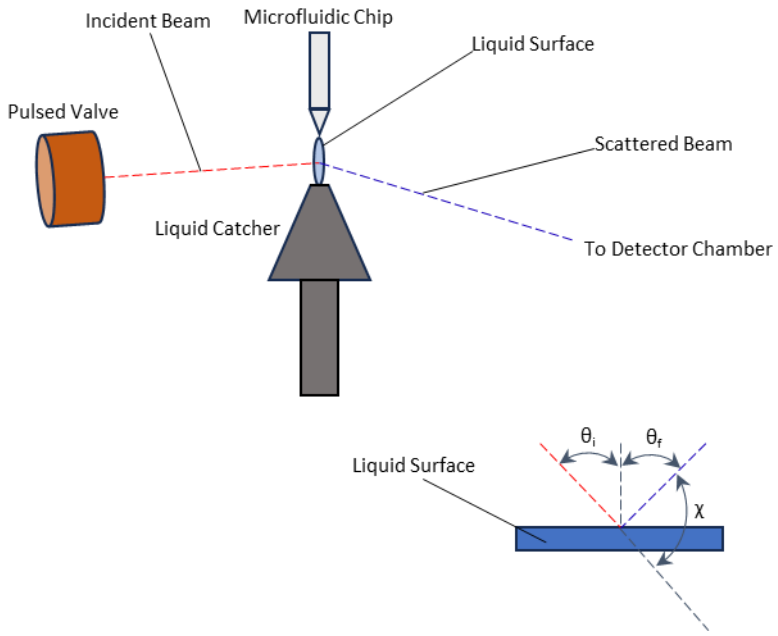


**Figure 6.3.1.** Instrument schematic for scattering experiments performed in these works. Inset in the bottom right shows the incident angle $\theta_i$, the scattering angle $\theta_f$ and the deflection angle $\chi$.

The $ND_3$ supersonic beam is prepared by seeding 1.5 % $ND_3$ (Sigma–Aldrich 99 % D) in helium. Stagnation conditions through the 500 $\mu$m diameter orifice of the valve are 288 K and 3000 Torr with an opening time of 12 $\mu$s. This results in a temporal width of 27$\mu$s measured at the detector. The velocity of the molecular beam is characterized by time-of-flight (TOF) measurements as described previously.[24, 25] The velocity of the $ND_3$ molecular beam was measured to be 1730 ± 205 m $s^{-1}$ (FWHM) corresponding to a mean translational kinetic energy of 28.8 kJ $mol^{-1}$.

The dodecane flat liquid jet is produced by flowing liquid dodecane ($n$-$C_{12}H_{26}$, TCI America #D0968) through a commercially available microfluidic chip (Micronit BV, Enschede)[40] as described in our previous works.[24, 25] Operating conditions include a flow rate of 3.5 mL $min^{-1}$ and corresponding flow velocity of 10 m $s^{-1}$, resulting in average dimensions of the flat jet of 1.0 × 4.5 $mm^2$ (W × H). The thickness of the jet is not directly measured but is estimated to be ~1.5 µm at its center.[24, 25] The average temperature of the liquid in both evaporation and scattering experiments was measured to be 269 K.

The 3 x 3 $mm^2$ detector aperture used throughout leads to a viewing time of ~0.5 ms for species detected during all experiments. TOF measurements are taken with the ionizer set to an electron kinetic energy of 80 eV. Each measurement is taken with an acquisition time between 2 and 8 minutes. Time zero for the evaporation experiments is determined by the rotating chopper wheel described prior,[24, 25] while time zero for scattering experiments is defined when the most intense part of the molecular beam collides with the flat liquid jet.

Evaporation experiments are performed by dissolving $ND_3$ in the dodecane reservoir. The dodecane reservoir is initially vacuum degassed for several minutes and then slowly over-pressurized to 850 Torr with the 1.5 % $ND_3$/He mixture. This process is repeated five times. In evaporation experiments, the molecular beam is not present. Scattering experiments are performed by vacuum degassing the dodecane reservoir as described for evaporation, but over-pressurized with pure helium instead of $ND_3$/He.

The incident angle $\theta_i$ is defined as the angle between the molecular beam axis and the liquid surface normal, which is set by rotation of the flat liquid jet assembly. In this work, incident angles of 45, 60, and 80° are chosen. The scattering angle $\theta_f$ is defined as the angle between the liquid surface normal the detector axis. The deflection angle $\chi$ is defined as $\chi = 180° - (\theta_i + \theta_f)$. A depiction of the scattering geometry can be seen in the inset of Fig. 6.3.1. In order to prevent systematic errors, TOF measurements are taken in a back-and-forth manner as described previously.[25]

# 6.4 Results and Discussion

## 6.4.1 Evaporation

Evaporation experiments are used to isolate the TD channel of the scattering experiments and ensure conditions are present for nascent scattering. During evaporation, the particles thermalize with the liquid, which results in a particle flux being described by a Maxwell–Boltzmann (MB) flux distribution.

$$f_{\mathrm{MB}}(v) \propto v^3 \exp\left(-\frac{mv^2}{2RT_{\mathrm{liq}}}\right) \#(1)$$

Here, $v$ and $m$ represent the velocity and mass of the evaporating particles, while $R$ is the universal gas constant. TOF profiles for the evaporation of $ND_3$ from a dodecane flat jet at detector angles $\theta_f$ = 0, 30, 60, and 90° are fitted using a linear combination of MB distributions and shown in Fig. 6.4.1.

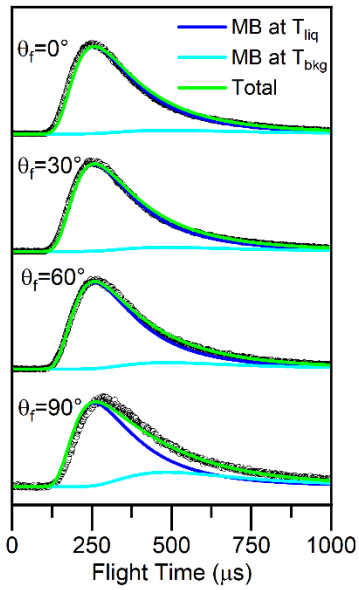


**Figure 6.4.1.** Normalized evaporation TOF spectra of $ND_3$ from a $ND_3$-doped liquid dodecane flat jet at 269 K. TOF distributions are fitted with a linear combination of Maxwell–Boltzmann velocity distributions at the liquid temperature (blue traces) and at $T_{bkg}$ = 75 K (light blue traces). The absolute intensity of the $T_{bkg}$ component is fixed for all angles. The green traces represent the sum of the two contributions.

The fitting procedure used in Fig. 6.4.1 has been described in our prior works.[24, 25] The blue and light blue traces in Fig. 6.4.1 show contributions to the TOF spectra that are described by an MB distribution at the liquid temperature $T_{liq}$ and background temperature $T_{bkg}$, respectively, and the green traces show the sum of these two distributions. The background contribution arises due to desorption of $ND_3$ from the Cu cryocooled wall in the collision chamber that has been experimentally measured to have a temperature of ~118 K in this study.

The TOF spectra for $\theta_f = 0°$ is well-fitted by the $T_{liq}$ MB distribution alone, while spectra at detector angles further away from the surface normal tend to display more "sub-Maxwellian" behavior and have a larger contribution from the $T_{bkg}$ distribution. This trend is explained by the relative flux of evaporated particles from the jet following a $\cos\theta_f$ distribution well-described in the literature.[41, 42]

Integrating the TOF spectra and plotting the intensity as a function of detector angle $\theta_f$ results in the angular plot shown in Fig. 6.4.2.

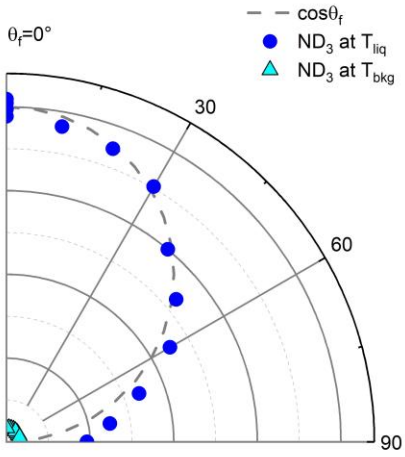


**Figure 6.4.2.** Angular plot created from the integrated, non-normalized intensities of the Maxwell–Boltzmann simulations at $T_{liq}$ and $T_{bkg}$ (blue circles and cyan triangles, respectively) of $ND_3$ evaporation data at various detector angles. The cosine function representing the expected angular distribution for evaporation is indicated by the dashed gray curve.

The angular plot in Fig. 6.4.2 shows the $T_{liq}$ MB distributions in dark blue circles, the $T_{bkg}$ MB distributions in light blue triangles, and the $\cos\theta_f$ distribution with a dashed curve. The $T_{liq}$ distribution is captured by the expected $\cos\theta_f$ distribution from the cosine law of evaporation. Maxwellian behavior of the TOF spectra as well as the $T_{liq}$ distributions fitting the expected $\cos\theta_f$ distribution suggest that $ND_3$ evaporation from the jet takes place without significant interference from vapor phase collisions, indicating that scattering experiments should result in nascent scattering from the surface of the flat liquid jet.[24, 25]

## 6.4.2 Scattering

While evaporation can be described by single mechanism in TD, scattering features more complicated mechanisms; however, this picture can be simplified significantly by confining the description of scattering to two mechanisms, TD and IS. Unlike TD, which is described by a MB distribution, IS is better described by a supersonic (SS) distribution due to the scattered particles maintaining more character of the incident supersonic molecular beam:[5, 27, 43, 44]

$$f_{SS}(v) \propto v^3 \exp\left(-\frac{m(v - v_{SS})^2}{2RT_{SS}}\right) \#(2)$$

where $v$ represents the velocity of the particle, $R$ is the universal gas constant, and $v_{SS}$ and $T_{SS}$ are the average flow velocity and average temperature of the molecular beam, respectively. TOF spectra of $ND_3$ scattering from a dodecane flat jet are shown in Fig. 6.4.3.

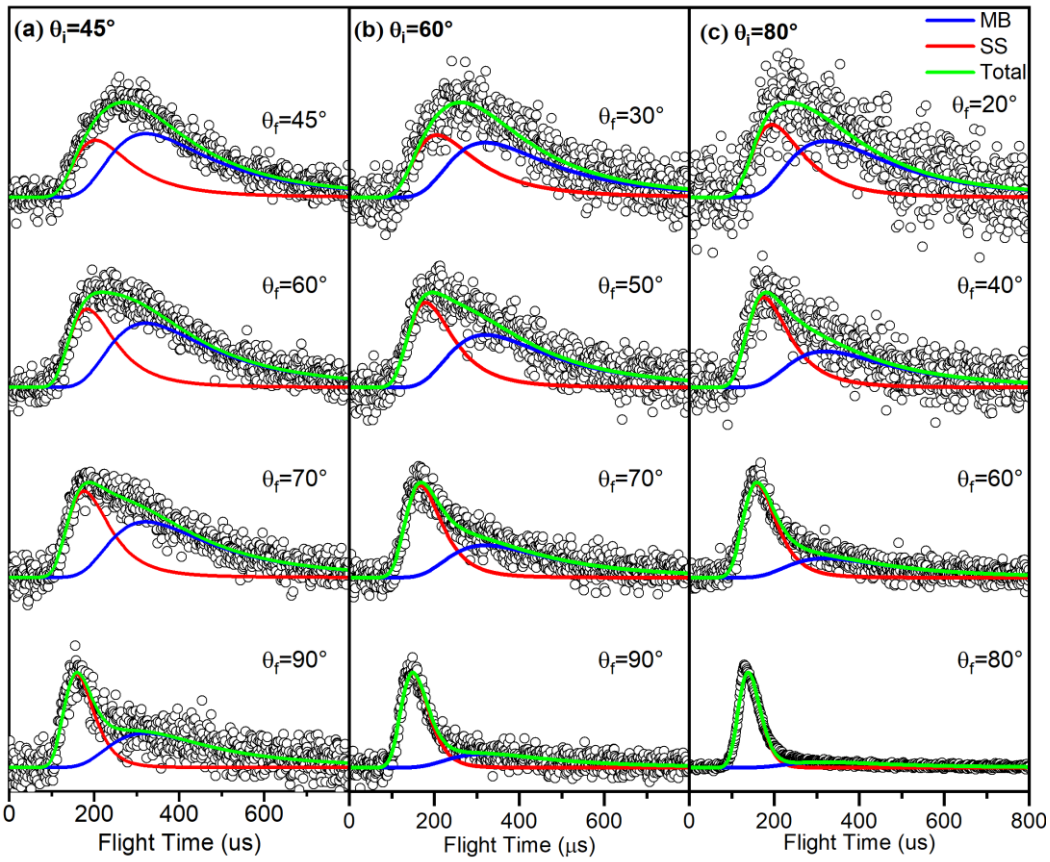


**Figure 6.4.3.** Normalized TOF spectra of $ND_3$ scattering ($E_i$ = 28.8 kJ mol$^{-1}$) from a dodecane flat liquid jet with (a) $\theta_i$ = 45°, (b) $\theta_i$ = 60°, and (c) $\theta_i$ = 80°. The data are fitted by the sum of an SS distribution (red traces) and an MB distribution (blue traces) at the liquid jet temperature ($T_{liq}$ = 269 K). The sum of the two contributions is shown by the green traces.

The TOF spectra in Fig. 6.4.3 are fitted with the MB distribution corresponding to the liquid temperature shown in blue, the SS distribution shown in red, and the sum of the two distributions shown in green. The blue trace corresponding to the MB distribution is representative of the fraction of the overall scattering events that result in TD, while the red trace corresponding to the SS distribution is representative of the overall scattering events that result in IS. A clear trend that persists in the data from Fig. 6.4.3 is that larger values of $\theta_f$ result in smaller TD fractions. This can be explained by the fact that at these angles the cosine law dictates that TD flux will be small.[45, 46] The trend for $\theta_i$ is similar as can be seen by comparing the three

spectra at the largest scattering angles. As $\theta_i$ increases, the scattering angle becomes more grazing in nature, also leading to smaller TD fractions.

TOF spectra from Fig. 6.4.3 were integrated to produce the angular plots shown in Fig. 6.4.4. The MB distributions corresponding to the TD mechanism are plotted on Fig. 6.4.4 as blue squares, the SS distributions corresponding to the IS mechanism are plotted as red circles, and the cosine distribution is once again plotted as a dashed curve. Additionally, each angular plot shows the specular angle as a large black arrow for reference. Overall, the MB distributions tend to follow a $\cos\theta_f$ trend as expected from TD. The SS distributions tend to peak in intensity near the specular angle for all three incident angles measured as expected of IS. However, the actual peak intensities for the $\theta_i$ = 45° and 60° angular plots occur at angles slightly larger than the specular angle. This "super-specular" scattering is well-known to occur in gas–solid scattering.[47, 48] This effect was also observed in our previous work on Ne, $CD_4$, and $D_2O$ and has been attributed to anisotropic momentum loss being favored parallel to the surface normal.[25]

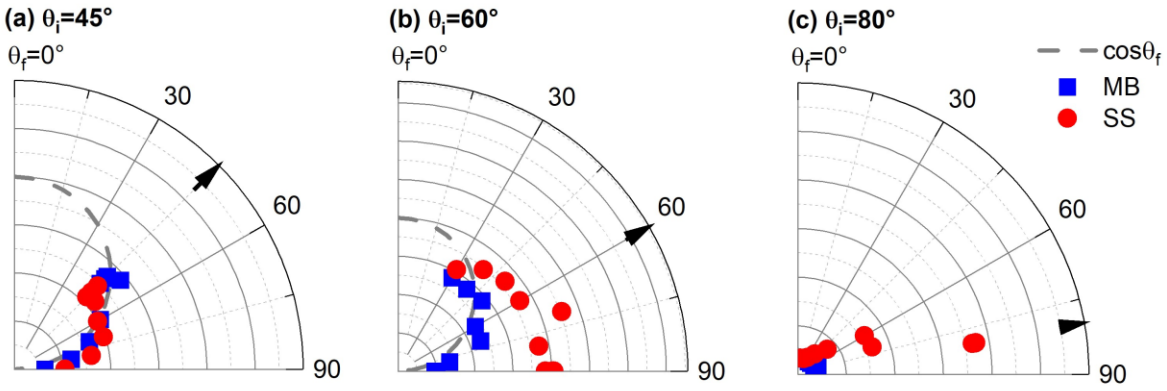


**Figure 6.4.4.** Angular plots created from the integrated, non-normalized intensities of scattering at incident angles of (a) 45°, (b) 60°, and (c) 80°. Blue squares represent the TD, and red circles represent the IS contributions to the TOF fits. The cosine function representing the expected angular distribution for evaporation is indicated by the dashed gray curves. Arrows indicate the specular angle.

## 6.4.3 Kinematic Models

The IS channel of scattering is fitted to a "soft-sphere" kinematic model. The soft-sphere model is well-described in the literature and allows for estimating the fractional energy loss of impulsively scattered molecules according to the equation below.[6, 49-51]

$$\left(\frac{\Delta E}{E_i}\right) \approx \frac{2\mu}{(1+\mu)^2}\left[1+\mu(\sin\chi)^2-\cos\chi\sqrt{1-\mu^2(\sin\chi)^2-\frac{E_{int}}{E_i}(\mu+1)}+\frac{E_{int}}{E_i}\left(\frac{\mu+1}{2\mu}\right)\right]\left[1+\frac{V-2RT_{liq}}{E_i}\right] \quad (3)\#$$

Where $\Delta E$ represents the change in translational energy of the scattered molecule. $E_i$ is the incident translational energy of the scattered molecule. The variable μ is the mass ratio between the scattered molecule and the effective surface mass $\mu = m_{gas}/m_{eff}$. The deflection angle is represented by $\chi$ as described above. $E_{int}$ is the total internal energy of both the scattered gas molecule and the liquid surface. $T_{liq}$ is the temperature of the liquid surface. $V$ represents the gas–surface potential calculated to be 2.8 kJ mol$^{-1}$ using combining rules on the Lennard-Jones parameters listed by Mourits and Rummens.[52, 53] Fractional energy loss as a function of deflection angle is plotted for $ND_3$ scattering in Fig. 6.4.6.

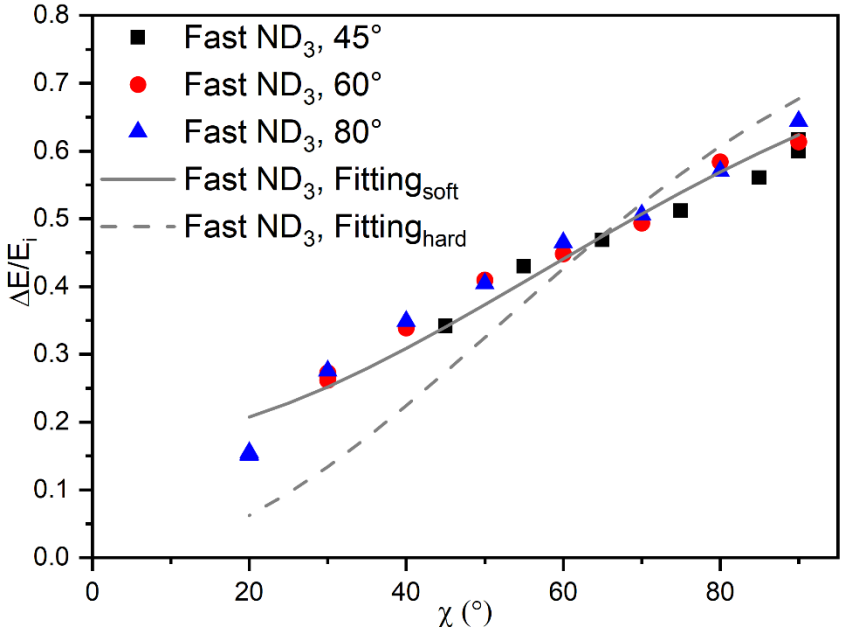


**Figure 6.4.6.** Average fractional energy loss as a function of deflection angle for impulsively scattered $ND_3$ from a dodecane flat jet at 269 K. The incident translational energy is 28.8 kJ mol$^{-1}$ and the gas-surface potential is modeled as 2.8 kJ mol$^{-1}$. The incident angles of 45°, 60°, and 80° are displayed as black squares, red circles, and blue triangles respectively. The data are fitted to the soft-sphere model represented by the solid gray curve, and the hard-sphere model represented by the dashed gray curve. The fitting parameters are $m_{eff}$ = 55 amu and $E_{int}$ = 5.08 kJ mol$^{-1}$ for the soft-sphere model, and $m_{eff}$ = 36 amu and $E_{int}$ = 0 kJ mol$^{-1}$ for the hard-sphere model.

$ND_3$ scattering on dodecane trends relatively well with the fitted soft-sphere model. Fractional energy loss increases with deflection angle as expected for all incident angles.[24, 25, 50] Similarly, the fractional energy loss is independent of incident angle for a given deflection angle. The effective surface mass as fitted by the soft-sphere model is 55 amu which corresponds to only a small portion of a dodecane molecule contributing to each $ND_3$ collision. The total

internal energy of the impulsively scattered $ND_3$ and surface was determined to be 5.08 kJ $mol^{-1}$ using the soft-sphere fitting model.

By assuming that the internal energy loss of the scattered species occurs entirely perpendicular to the surface normal, $E_{int}$ is used to calculate an estimation of the super-specular scattering angles. This analysis results in an increase of ~10° from specular for each angle of $ND_3$ scattered on a dodecane surface. This number matches well with the $\theta_i$ = 60° plot from Fig. 6.4.4 where the angle of maximum intensity appears to be approximately 70°, but does not match well with incident angles of 45° and 80°. This discrepancy is explained in our previous work, where it is mentioned that low signal to noise at 45° and contamination from non-scattered species entering the detector directly from our molecular beam at 80° provide the most likely explanation for this difference.[25]

Fractional energy loses for the scattering of Ne, $CD_4$, $D_2O$, and $ND_3$ on dodecane as well as Ne, $CH_4$, $D_2O$, and $NH_3$ scattered on squalane at $\chi$ = 90° are shown in Table 6.4.1.

**Table 6.4.1.** TD fractions and fractional energy losses for scattered molecules on a dodecane flat liquid jet and a squalane wetted wheel. Incident beam energies are 23.7, 29.3, 33.4, and 28.8 kJ $mol^{-1}$ for Ne, $CD_4$, $D_2O$, and $ND_3$ respectively. Potential energy well depths are 0.9, 1.9, 3.6, and 3.6 kJ $mol^{-1}$ for Ne, $CD_4$, $D_2O$, and $ND_3$ respectively. All values are taken from a deflection angle of 90°. $CD_4$ and $ND_3$ data for squalane is taken from the analogous species $CH_4$ and $NH_3$.Data for Ne, $CD_4$, and $D_2O$ on dodecane are taken from our previous work.[25] Data on squalane are taken from work performed by Nathanson[28] and interpolated to yield values at the appropriate beam energy for each species.

| | Fractional Energy Loss | | TD Fraction | |
|---|---|---|---|---|
| **Scattered Species** | **Dodecane** | **Squalane** | **Dodecane** | **Squalane** |
| Ne (Fast) | 0.46 | 0.42 | 0.28 | 0.30 |
| $CD_4$ | 0.61 | 0.49 | 0.44 | 0.50 |
| $D_2O$ | 0.64 | 0.56 | 0.50 | 0.58 |
| $ND_3$ | 0.62 | 0.51 | 0.54 | 0.63 |

The average translational energies of each species range from 23.7 to 33.4 kJ $mol^{-1}$ and are all measured at a deflection angle of 90°. The fractional energy losses of Ne, $CD_4$, $D_2O$, and $ND_3$ scattered on dodecane are compared to the analogous species scattered on squalane by Nathanson.[28] The ordering of the fractional energy loss for each scatterer is Ne < $CD_4$ < $ND_3$ < $D_2O$ on both squalane and dodecane.

In order to assess the degree of vibrational excitation, the percentage of molecules populating each vibrational mode was calculated at 269 K. Using the soft-sphere fitted internal

energy parameter of 5.08 kJ $mol^{-1}$, population analysis suggests that 93% of scattered $ND_3$ molecules are in their ground vibrational state. The umbrella inversion mode represents the largest fraction of vibrationally excited molecules and comprised a maximum of 6% of all scattered $ND_3$ molecules. While significantly more vibrational excitation occurs for $ND_3$ when compared to the previously studied species scattered on a liquid dodecane surface, most internal energy is still partitioned into rotational excitation as opposed to vibrations.

### 6.4.4 TD Fractions

The TD fraction is defined as the fraction of overall scattering events attributed to thermal desorption. TD fractions are shown in Table 6.4.1 and follow a similar trend to the data obtained by Nathanson for squalane, where the TD fraction of Ne is significantly smaller than that of the other scattered species.[28] The overall trend of TD fractions is Ne < $CD_4$ < $D_2O$ < $ND_3$ on both dodecane and squalane. Ne has a significantly smaller TD fraction than the molecular scatterers, while $CD_4$, $D_2O$, and $ND_3$ all have similar TD fractions. The increasing trend of the molecular scatterer TD fraction follows and has been attributed to the solubility of these molecules and the free energy of solvation $\Delta G^{\circ}_{Solv} = -RTlnK_H$ in previous work.[25, 28] As seen previously, the higher the solubility of the scattered species in dodecane, the higher the TD fraction. Comparing the TD fraction of species scattered on dodecane to Nathanson's work on squalane shows that for all species besides Ne there is a ∼15 % increase in TD fraction on squalane compared to dodecane; this trend is attributed to squalane being a softer surface than dodecane as mentioned in our previous work.[25]

## 6.5 Conclusions

The evaporation and scattering of $ND_3$ from a dodecane flat liquid jet is investigated and compared to previous work for Ne, $CD_4$, and $D_2O$ scattered from a dodecane flat liquid jet, as well as analogous species scattered from squalane on a wetted wheel. Evaporation experiments were performed to quantify the role that vapor phase interference would pose while scattering $ND_3$ from a dodecane flat jet. TOF measurements of $ND_3$ evaporation were fit to a sum of two MB distributions comprised of a fast contribution from evaporation and a slow contribution from the constant background signal. Good agreement between the MB fittings suggests that vapor phase interference does not contribute significantly to the measured evaporation signal.

Scattering experiments were conducted and followed similar trends seen in both our previous work and work by Nathanson on squalane. The angular plots for $ND_3$ scattering show that the TD channel for all incident angles obey the $\cos\theta_f$ law quite well, and the IS channel peaks at or slightly above the specular scattering angle for all three incident angles as expected from previous liquid surface scattering experiments. The TD fractions of the scattered species show that Ne has similar TD fractions on both dodecane and squalane, while $CD_4$, $D_2O$, and $ND_3$

have significantly higher TD fractions. The TD fractions of $CD_4$, $D_2O$, and $ND_3$ on squalane are ~15 % higher than the analogous scattered species on dodecane indicating that squalane is a softer surface than dodecane and therefore is more likely to trap scattered species.

The fractional energy losses for $ND_3$ agree quite well with the soft-sphere model fitting presented in Fig. 6.4.6 at all three incident angles. When comparing the fractional energy losses of all scattered species, the fractional energy loss on dodecane and squalane follow the trend of $Ne < CD_4 < ND_3 < D_2O$. The fractional energy loss of 0.62 for $ND_3$ on dodecane follows the trend of the other polyatomic species and is ~10 % greater than the analogous species scattered from squalane.

This work concludes our investigation of small molecule scattering from a dodecane flat-jet, and in conjunction with our previous work serves as a proof of concept of elucidating small molecule scattering dynamics from a volatile flat liquid jet. Future directions of this work aim to investigate both non-reactive and reactive scattering of more volatile liquids such as water.

# 6.6 Acknowledgements

The authors acknowledge the support provided by the Office of Basic Energy Science, Chemical Sciences Division of the U.S. Department of Energy under Contract No. DE-AC02-05CH11231. The authors acknowledge Bernd Winter, Bernd Abel, and Manfred Faubel for helpful discussions in the early phases of this work.

# 6.7 References

[1] A. Singh, and M. Agrawal, Journal of Environmental Biology **29** (2007) 15.
[2] R. Putikam, and M. C. Lin, Int. J. Quantum Chem. **118** (2018) e25560.
[3] M. F. Ruiz-Lopez *et al.*, J. Am. Chem. Soc. **141** (2019) 16564.
[4] D. Phillips, (University of East Anglia, 2022).
[5] M. E. Saecker *et al.*, Science **252** (1991) 1421.
[6] G. M. Nathanson, Annu Rev Phys Chem **55** (2004) 231.
[7] J. A. Faust, and G. M. Nathanson, Chem Soc Rev **45** (2016) 3609.
[8] D. Herschbach, Faraday Discussions of the Chemical Society **55** (1973) 233.
[9] D. Neumark *et al.*, The Journal of chemical physics **82** (1985) 3045.
[10] R. Continetti, B. Balko, and Y. T. Lee, The Journal of chemical physics **93** (1990) 5719.
[11] W. H. Weinberg, Advances in Colloid and Interface Science **4** (1975)
[12] J. Hurst *et al.*, Physical review letters **43** (1979) 1175.
[13] J. A. B. a. D. J. Auerbach, Surface Science **4** (1985)
[14] U. Harten *et al.*, Physical review letters **54** (1985) 2619.
[15] M. J. Cardillo, Surface Science (1994)

[16] Y. Huang *et al.*, Science **290** (2000) 111.
[17] M. E. King *et al.*, Physical review letters **70** (1993) 1026.
[18] P. D. Gilbert M. Nathanson, Douglas R. Worsnop, Charles E. Kolb, Journal of Physical Chemistry **100** (1996)
[19] J. Z. Bohan Wu, Timothy K. Minton, Kenneth G. McKendrick, John M. Slattery, Scott Yockel, George C. Schatz, Journal of Physical Chemistry **114** (2010)
[20] S. M. Brastad, and G. M. Nathanson, Phys. Chem. Chem. Phys. **13** (2011) 8284.
[21] P. D. Lane *et al.*, J. Phys. Chem. C **124** (2020) 16439.
[22] S. S. M. Faubel, and J.P. Toennies, Atoms, Molecules, and Clusters **10** (1988)
[23] M. Faubel, and T. Kisters, Nature **339** (1989) 527.
[24] C. Lee *et al.*, J Phys Chem A **126** (2022) 3373.
[25] W. Yang *et al.*, J Chem Phys **159** (2023)
[26] K. C. J. J. E. H. J. C. L. Warton, Surface Science **130** (1982)
[27] I. Kinefuchi *et al.*, Microfluidics and Nanofluidics **21** (2017)
[28] M. E. Saecker, and G. M. Nathanson, The Journal of Chemical Physics **99** (1993) 7056.
[29] R. B. Paul J. Hesse, Pirketta Scharlin, Emmerich Wilhelm, Journal of Chemical Enginering Data **41** (1996)
[30] P. Schatzberg, Journal of Physical Chemistry **67** (1962)
[31] D. C. Ghosh, J. Jana, and R. Biswas, Int. J. Quantum Chem. **80** (2000) 1.
[32] C. A. U.-D. Jorge Ricardo Letelier, Spectrochimica Acta Part A **53** (1997)
[33] P. L. A. P. Nathaniel O.J. Malcolm, Journal of Physical Chemistry A **105** (2001)
[34] T. Shimanouchi, *Tables of Molecular Vibrational Frequencies* 1976), Vol. 1,
[35] K. Ishida, Bulletin Chemical Society of Japan **31** (1958)
[36] Y.-T. Lee *et al.*, Review of Scientific Instruments **40** (1969) 1402.
[37] Y. T. Lee, Angew. Chem., Int. Ed. Engl. **26** (1987) 939.
[38] D. Irimia *et al.*, Review of Scientific Instruments **80** (2009)
[39] C. Meng, and M. H. Janssen, Review of Scientific Instruments **86** (2015)
[40] J. D. Koralek *et al.*, Nat. Commun. **9** (2018) 1353.
[41] E. H. Kennard, *Kinetic theory of gases* (McGraw-hill New York, 1938), Vol. 483,
[42] Z. R. Kann, and J. L. Skinner, J Chem Phys **144** (2016) 154701.
[43] F. B. Dunning, and R. G. Hulet, *Atomic, molecular, and optical physics: Atoms and molecules* (Academic press, 1996),
[44] A. Lebéhot *et al.*, Atomic and Molecular Beams: The State of the Art 2000 (2001) 237.
[45] K. M. F. Mackenzie E. King, Gilbert Nathanson, Journal of Physical Chemistry **101** (1997)
[46] D. J. N. Bradford G. Perkins Jr., Journal of Physical Chemistry **113** (2009)
[47] R. Subbarao, and D. Miller, The Journal of Chemical Physics **58** (1973) 5247.
[48] C. Rettner, L. DeLouise, and D. Auerbach, The Journal of chemical physics **85** (1986) 1131.
[49] C. T. Rettner, and M. N. R. Ashfold, (No Title) (1991)
[50] W. A. Alexander *et al.*, Faraday discussions **157** (2012) 355.
[51] N. Andric, and P. Jenny, Physics of Fluids **30** (2018)
[52] F. M. M. a. F. H. A. Rummens, Can. J. Chem. **55** (1977)
[53] H. A. Lorentz, Annals of Physics (1881)

# Appendix

# A1. ISOPOOH Synthesis Modifications

The ISOPOOH synthesis largely follows the procedure outlined in the thesis by Lozano with the exception of two steps:

1. The step that calls for stirring methanol and hydrogen peroxide overnight was done for 3 hours instead.

2. The hydrogen peroxide in the last step was added dropwise via pipette over the course of 10 minutes while the reaction mixture was suspended in a regular ice bath.

# A2. Liquid Jet Scattering Data Analysis Python Code

## File 1: Molecular Beam

```
################################################################################
#
# <INTRO>:                                                    #
# This script is used to fit the molecular beam profile using supersonic (SS) #
# distribution . It gives the fitting parameters of temperature (T) and flow  #
# velocity (v0). These numbers should be used in the scattering data for      #
# convolution.                                                #
#                                                             #
# <INPUT>:                                                    #
# The input data should be full molecular beam profile detected without       #
# chopper wheel in at detector angle at 270deg. Each data should include beam #
# on and off with time interval of 1 us. The MCS delay is default to be set at#
# the same delay as scattering data MCS delay. If MCS delay is 1250us, this   #
# number can be adjust at parameter "dMCSdelay". Th input data should be saved#
# in a folder, which is at the same file path as the script.                  #
#                                                             #
# <OUTPUT>:                                                   #
# The output data are in the variables. Only the important ones are shown:    #
#                                                             #
#    xData:        flight time (us)                           #
#    yDataRaw:     data from the input file                   #
#    yData:        yDataRaw with beam on/off subtraction      #
#    yData_norm:   normalizeation of yData                    #
#    yFit_SS:      fitted supersonic profile of yData         #
```

```
#    yFit_SS_norm:  normalizeation of yFit_SS                          #
#    yFit_SS_param: parameters of yFit_SS                              #
#                                                                      #
#    E_mean:        translational energy of the beam (kJ/mol)          #
#                                                                      #
#    beam_E:        average value of translational energy of the beam (kJ/mol)#
#    beam_T:        average value of fitted beam temperature (K)       #
#    beam_v0:       average value of fitted flow velocity (m/s)        #
#                                                                      #
# <OUTLINE>:                                                           #
#      Parameters                                                      #
#    0. Initialize Enviornment                                         #
#    1. Data Loading                                                   #
#    2. Normalization and Plotting                                     #
#    3. Mean Translational Energy                                      #
#    4. Data Processing                                                #
########################################################################################
#



##########----------PARAMETERS----------##########
folderName = "ND3_80deg_combined" # name of the folder that includes molecular beam data
beamName = "Fast ND3"         # name of the beam
L = 0.1716+0.036              # m, flight distance, default should be 0.1716+0.036 cm
```

```
dMCSdelay = 0                # us, if the molecular beam profile are taken using scattering MCS delay time, put 0us. If the MCS delay time is, put (1250-scattering MCS delay time).


# Supersonic (SS) distribution fitting parameters
m = 20          # amu, parent ion mass
m_ion = 20      # amu, daughter ion mass
dm = 0.0001     # amu
T = 0           # K, fitting temperature parameter for SS
dT = 1000       # K
v0 = 0          # m/s, fitting flow velocity parameter for SS
dv0 = 2000      # m/s
##########------------------------------------------------------------##########




##########----------------0. Initialize Enviornment----------------##########
#from IPython import get_ipython
#get_ipython().magic('reset -sf')

import pathlib
import matplotlib.pyplot as plt
from scipy.optimize import curve_fit
import numpy as np
import math
import os
##########------------------------------------------------------------##########
```

```
##########----------1. Data Loading----------##########
# Function to load data
def LoadData(folderName):
    filePath = str(pathlib.Path().resolve())+str("\\")+folderName
    fileName = os.listdir(filePath)
    yDataRaw = []
    for i in range(len(fileName)):
        file = os.path.join(filePath , fileName[i])
        yDataRaw.append(np.loadtxt(file))
    return fileName, yDataRaw

# Function do beam subtraction
def Subtract(yDataRaw):
    count = int(len(yDataRaw))
    yData = []
    for i in range(count):
        length = int(len(yDataRaw[i])/2)
        y = [yDataRaw[i][j] - yDataRaw[i][j+length] for j in range(length)]
        yData.append(y)
    return yData

# Load raw data into Python. Prepare xData and yData with time offset and beam on/off
subtraction.
fileName, yDataRaw = LoadData(folderName)
```

```
yData = Subtract(yDataRaw) # If the raw data include beam on and off, use "Subtract" function to do beam subtraction

t_offset = (-6 + 19.5 + 4.8*(m_ion)**0.5) - dMCSdelay # the MCS delay is setted wrong

xData = np.array([i - t_offset for i in range(len(yData[0]))])


Nfile = len(fileName) # int, number of files

NxData = len(xData)   # list, number of x in xData

##########----------------------------------------------------------##########




##########----------2. Normalization and Plotting----------##########

# Define supersonic (SS) distribution

def SS(t, m, T, A, v0):

    temp = (1/(t*10**-6)**4)*np.exp(-m/1000/(2*8.314*T)*(L/(t*10**-6)-v0)**2)

    Dist = temp/np.max(temp)

    Dist = A*Dist

    return Dist


# Fit molecular beam profile with SS distribution

yFit_SS = []

yFit_SS_param = []

for i in range(Nfile):

    y = yData[i]


    popt_SS,pcov_SS = curve_fit(SS,xData,y,bounds=([m,T,0,v0],[m+dm,T+dT,100000,v0+dv0]))
```

```
    yFit_SS.append(SS(xData,*popt_SS))
    yFit_SS_param.append(popt_SS)

# Plotting
plt.figure(figsize=(8,6))
for i in range(Nfile):
    plt.subplot(1, math.ceil(Nfile/1), i+1)

    plt.plot(xData,yData[i],  'ko',markersize=1,label='Data')
    plt.plot(xData,yFit_SS[i],'r-',markersize=1,label='SS')
    plt.xlim(0,400)
    plt.xlabel('Flight Time (us)')
    plt.title("[1]\n ([2])".format(beamName,fileName[i]),fontsize=10)
    plt.text(380,1000,"T =  {:.2f} K    \n v0 ={:.2f}
m/s".format(yFit_SS_param[i][1],yFit_SS_param[i][3]),horizontalalignment='right',fontsize=8)
plt.tight_layout()
plt.legend()

# Print fitted beam temperature (T) and flow velocity (v0)
beam_T =  sum([yFit_SS_param[i][1] for i in range(Nfile)])/Nfile
beam_v0 = sum([yFit_SS_param[i][3] for i in range(Nfile)])/Nfile

print("Average beam temperature (T)  =  %.4f K" % beam_T)
print("Average flow velocity    (v0) = %.4f m/s" % beam_v0)
##########------------------------------------------------------------##########
```

```
##########----------3. Mean Translational Energy----------##########
# Calculate fitted SS's E_mean (unit=kJ/mol) and S=(speed ratio)**2
E_mean = []
S = []
xTime = [i for i in range(1,2501)]            # unit: us
xVelocity = [L/(t*10**-6) for t in xTime]     # unit: m/s
yEnergy = [0.5*m/1000*v**2 for v in xVelocity] # unit: J/mol
for i in range(Nfile):
    m = yFit_SS_param[i][0]
    T = yFit_SS_param[i][1]
    v0 = yFit_SS_param[i][3]

    # Below, SS function in the velocity space is used for yIntensity. No Jacobian is required. See Comsa's 1985 paper
    yIntensity = [1/T*np.exp(-m/1000*(v-v0)**2/(2*8.314*T))*v**3 for v in xVelocity]

    E_temp_1 = [(xVelocity[j]-xVelocity[j+1])*(yIntensity[j]+yIntensity[j+1])/2*(yEnergy[j]+yEnergy[j+1])/2 for j in range(int(len(xVelocity)-1))]
    E_temp_2 = [(xVelocity[j]-xVelocity[j+1])*(yIntensity[j]+yIntensity[j+1])/2 for j in range(int(len(xVelocity)-1))]
    E_mean_temp = sum(E_temp_1)/sum(E_temp_2)/1000 # kJ/mol
    E_mean.append(E_mean_temp)

    S_temp=yFit_SS_param[i][0]/1000*yFit_SS_param[i][3]**2/(2*8.314*yFit_SS_param[i][1])
    S.append(S_temp)

# Print fitted beam temperature (T) and flow velocity (v0)
beam_E =  sum([E_mean[i] for i in range(Nfile)])/Nfile
```

```
print("Average beam energy (E)  =  %.2f kJ/mol" % beam_E)
##########----------------------------------------------------------##########



##########--------------------4. Data Processing--------------------##########
# Normalize yData and yFit_SS for data plotting in origin
yData_norm = [[i/max(yFit_SS[j]) for i in yData[j]]for j in range(Nfile)]
yFit_SS_norm = [[i/max(yFit_SS[j]) for i in yFit_SS[j]]for j in range(Nfile)]

# Reshaping the data for easy copying
yDataRaw = np.reshape(yDataRaw,(Nfile,int(NxData*2))).T
yData = np.reshape(yData,(Nfile,NxData)).T
yData_norm = np.reshape(yData_norm,(Nfile,NxData)).T
yFit_SS = np.reshape(yFit_SS,(Nfile,NxData)).T
yFit_SS_norm = np.reshape(yFit_SS_norm,(Nfile,NxData)).T
yFit_SS_param = np.reshape(yFit_SS_param,(Nfile,np.size(yFit_SS_param[0]))).T



##########--------------------5. FWHM Calculation--------------------##########
def lin_interp(x, y, i, half):
    return x[i] + (x[i+1] - x[i]) * ((half - y[i]) / (y[i+1] - y[i]))

def half_max_x(x, y):
    half = max(y)/2.0
    signs = np.sign(np.add(y, -half))
```

```
    zero_crossings = (signs[0:-2] != signs[1:-1])
    zero_crossings_i = np.where(zero_crossings)[0]
    return [lin_interp(x, y, zero_crossings_i[0], half),
            lin_interp(x, y, zero_crossings_i[1], half)]

for i in range(Nfile):
    x=xData
    y=yData[:,i]

# find the two crossing points
    hmx = half_max_x(x,y)

# fwhm time domain
    fwhm = hmx[1] - hmx[0]
    #print("FWHM:{:.3f}".format(fwhm))

# beam velocity
    beam_vel = L*1e6/xData[np.argmax(yData[:,i])]
    print("Beam velocity = {:.3f}".format(beam_vel))

# fwhm bounds
    [fwhm_min, fwhm_max] = [xData[np.argmax(yData[:,i]) - round(fwhm/2)],
xData[np.argmax(yData[:,i]) + round(fwhm/2)]]
    [beam_vel_min, beam_vel_max] = [L*1e6/fwhm_max, L*1e6/fwhm_min]
    print("Beam velocity min = {:.3f}".format(beam_vel_min))
    print("Beam velocity max = {:.3f}".format(beam_vel_max))

# fwhm velocity space
```

```
    fwhm_vel = (beam_vel_max - beam_vel_min)/2
    print("FWHM = {:.3f}".format(fwhm_vel))


#plot (in repair)
    # half = max(y)/2.0
    # plt.plot(x,y)
    # plt.plot(hmx, [half, half])
plt.show()


# Deleting parameters that are not important. If wish to debug, unfunction this line.
del
beamName,dm,dT,dv0,dMCSdelay,E_mean_temp,E_temp_1,E_temp_2,fileName,folderName,i,
L,m,m_ion,Nfile,NxData,pcov_SS,popt_SS,T,t_offset,v0,xVelocity,y,yEnergy,yIntensity
##########------------------------------------------------------------##########
```

## File 2: Energy Transfer

```
#############################################################################################
#
# <INTRO>:                                                  #
# This script is used to fit energy transfer parameters of soft and hard      #
# sphere model. The fitted parameters are mass ratio (mu) and total internal  #
# excitation (Eint).                                        #
#                                                       #
# <INPUT>:                                                  #
# No files are required for this code. Only that the parameters need to be    #
# filled up before calculating it, which the numbers can be pre-fit and found #
# in "Molecular Beam.py" and "xxx_xxdeg.py".                          #
#                                                       #
```

```
# <OUTPUT>:                                                    #
# The output data are in the variables. Only the important ones are shown:    #
#                                                              #
#    xChi:                    deflection angle (degree)              #
#    yE_transfer:               energy transfer (ratio)               #
#                                                              #
#    xChi_Fit:                deflection angle for yE_transfer_Fit (degree)#
#    yE_transfer_Fit_hard:       fitted energy transfer with hard sphere model#
#    yE_transfer_Fit_hard_param: parameters of yE_transfer_Fit_hard          #
#    yE_transfer_Fit_soft:       fitted energy transfer with soft sphere model#
#    yE_transfer_Fit_soft_param: parameters of yE_transfer_Fit_soft          #
#                                                              #
# <OUTLINE>:                                                     #
#       Parameters                                           #
#    0. Initialize Enviornment                                   #
#    1. Data Converting                                        #
#    2. Energy Transfer Fitting and Plotting                          #
#    3. Data Processing                                       #
################################################################################
#
```

```
##########----------------------PARAMETERS----------------------##########
Theta_i = [   45,   60,   80] # degree, incident angle
T_liq   = [  269,  269,  269] # K,      liquid temperature
```

```
E_i     = [29.31,29.31,29.385] # kJ/mol, incident beam energy


m_g = 20 # amu, mass of incident gas


xAngle = [[45,60,80,90,45,70,50,45],       # degree, outgoing angle
        [90,70,50,30,90,40,60,80,90],
        [80,60,40,20,80,10,30,50,70,80]] # exclude 90deg


yE_SS = [[11.85025,13.36893,17.01061,18.93996,11.21622,15.50526,12.39072,11.14406],
# kJ/mol, mean translational energy of suparsonic part (E_mean)
       [21.65629,17.57041,14.80855,11.46618,21.59380,12.89372,16.04659,19.50314,21.58138],

[24.83455,19.39334,15.74812,12.91898,24.78267,11.27028,14.35635,17.22181,21.36080,24.77
978
]]
##########----------------------------------------------------------##########




##########----------0. Initialize Enviornment----------##########
from IPython import get_ipython
#get_ipython().magic('reset -sf')


import matplotlib.pyplot as plt
from scipy.optimize import curve_fit
import numpy as np
```

```
##########----------------------------------------------------------##########



##########----------------------1. Data Converting--------------------##########
# Also fit a "total" fit for all the Theta_i
Nfile=len(Theta_i)
Name = ['{}deg'.format(Theta_i[i]) for i in range(Nfile)]
Name.append('Total')

T_liq.append(sum(T_liq)/len(T_liq))
E_i.append(np.average(E_i))

# Convert outgoig angle(xAngle) to deflection angle(xChi)
xChi     = [180-Theta_i[i]-np.array(xAngle[i]) for i in range(Nfile)]
xChi.append(np.array(np.concatenate(xChi)))

# Convert translational energy of supersonic part(yE_SS) to energy transfer(yE_transfer)
yE_transfer = [(E_i[i]-np.array(yE_SS[i]))/E_i[i] for i in range(Nfile)]
yE_transfer.append(np.array(np.concatenate(yE_transfer)))
##########----------------------------------------------------------##########



##########----------2. Energy Transfer Fitting and Plotting----------##########
# Function to calculate energy transfer
# Ei's unit: kJ/mol; mu's unit: non(ratio); Eint's unit: kJ/mol; T_liq's unit: K
```

```
def Energy_Transfer(X, Ei, mu, Eint, T_liq): #from Minton's 2012 paper equation (7)
    X = X/360*2*np.pi
    f = (2*mu/(mu+1)**2)*(1+mu*np.sin(X)**2+Eint/Ei*((mu+1)/(2*mu))-np.cos(X)*(1-
mu**2*np.sin(X)**2-Eint/Ei*(mu+1))**0.5)
    E = (1+(1.9-2*8.314*T_liq/1000)/Ei)
    result = f*E
    return result


# Fitting and plotting
Colors=['k','r','b','g']
plt.figure(figsize=(8,6))


xChi_Fit=[]
yE_transfer_Fit_soft=[]
yE_transfer_Fit_hard=[]
yE_transfer_Fit_soft_param=[]
yE_transfer_Fit_hard_param=[]
for i in range(Nfile+1):
    x = xChi[i]
    y = yE_transfer[i]


    popt_soft,pcov_soft = curve_fit(Energy_Transfer,x,y,p0=[E_i[i], 0.1, 5,
T_liq[i]],bounds=([E_i[i], 0.0001, 0.0001, T_liq[i]],[E_i[i]+0.0001, 10, 30,      T_liq[i]+0.0001]))
    popt_hard,pcov_hard = curve_fit(Energy_Transfer,x,y,p0=[E_i[i], 0.1, 0,
T_liq[i]],bounds=([E_i[i], 0.0001, 0     , T_liq[i]],[E_i[i]+0.0001, 10,  0.0001, T_liq[i]+0.0001]))
    yE_transfer_Fit_soft_param.append(popt_soft)
    yE_transfer_Fit_hard_param.append(popt_hard)
```

```
    xChi_Fit_temp = np.arange(max(x),min(x)-5,-5)
    xChi_Fit.append(xChi_Fit_temp)
    yE_transfer_Fit_soft_temp = Energy_Transfer(xChi_Fit_temp,*popt_soft)
    yE_transfer_Fit_hard_temp = Energy_Transfer(xChi_Fit_temp,*popt_hard)
    yE_transfer_Fit_soft.append(yE_transfer_Fit_soft_temp)
    yE_transfer_Fit_hard.append(yE_transfer_Fit_hard_temp)


    plt.plot(x,y,'o',color=Colors[i],label=Name[i])
    plt.plot(xChi_Fit_temp,yE_transfer_Fit_soft_temp,'-',color=Colors[i],label='Fitting for
{}_soft'.format(Name[i]))
    plt.plot(xChi_Fit_temp,yE_transfer_Fit_hard_temp,'--',color=Colors[i],label='Fitting for
{}_hard'.format(Name[i]))
plt.legend()


# Print out soft and hard sphere's fitting parameters for total fitting
print('Soft Sphere Fitting:')
print('   Effective surface mass is %.2f amu' % float(m_g/popt_soft[1]))
print('   Eint/Ei is %.2f' % float(popt_soft[2]/popt_soft[0]))
print('   Eint is %.2f kJ/mol' % float(popt_soft[2]))
print('Hard Sphere Fitting:')
print('   Effective surface mass is %.2f amu' % float(m_g/popt_hard[1]))
print('   Eint/Ei is %.2f, (should be close to zero)' % float(popt_hard[2]/popt_hard[0]))
print('   Eint is %.2f kJ/mol, (should be close to zero)' % float(popt_hard[2]))
##########------------------------------------------------------------##########



##########----------3. Data Processing----------##########
```

```
yE_transfer_Fit_soft_param =
np.reshape(yE_transfer_Fit_soft_param,(int(Nfile+1),len(yE_transfer_Fit_soft_param[0]))).T

yE_transfer_Fit_hard_param =
np.reshape(yE_transfer_Fit_hard_param,(int(Nfile+1),len(yE_transfer_Fit_hard_param[0]))).T


# Deleting parameters that are not important. If wish to debug, unfunction this line.

del
Colors,E_i,i,m_g,Name,Nfile,pcov_hard,pcov_soft,popt_hard,popt_soft,T_liq,Theta_i,x,xAngle,
xChi_Fit_temp,y,yE_SS,yE_transfer_Fit_hard_temp,yE_transfer_Fit_soft_temp

##########------------------------------------------------------------##########
```